Journal of Volcanology and Geothermal Research 419 (2021) 107380

Contents lists available at ScienceDirect

Journal of Volcanology and Geothermal Research

journal homepage: www.elsevier.com/locate/jvolgeores

Invited research article

Making the most of the Mogi model: Size matters

Nicola C. Taylor *, Jessica H. Johnson, Richard A. Herd

School of Environmental Sciences, University of East Anglia, Norwich, UK

ARTICLE INFO

Article history:
Received 11 May 2020
Received in revised form 5 August 2021
Accepted 18 August 2021
Available online 24 August 2021

Keywords:
Mogi
McTigue
Finite element models
Kīlauea
Deformation

ABSTRACT

Magma movements are almost universally associated with volcanic deformation. The Mogi (1958) and McTigue (1987) models link observed surface displacements to behaviour within inaccessible magmatic plumbing systems. Mogi and McTigue models are well-used due to their computational simplicity and ease of application, but both models are limited by their assumptions about the deformation source and its embedding domain. Domain assumptions, including elasticity, homogeneity, and flat topography, have been previously described and corrected for. Whilst recognising the limits of these models, their frequent use in the literature requires an objective assessment of their utility against more sophisticated Finite Element (FE) models, their operational limits (radius-to-depth ratio, ε) and their relative merits in the light of limited field data. Here, we relax the source assumption of a small ε. We simulate volcanic deformation using Mogi, McTigue and FE models - the latter unrestricted by ε - to validate the maximum ε for which the analytical models can be applied, and to compare analytical and FE interpretations of deformation data from Kīlauea Volcano, Hawai'i. We find that analytical and FE models correspond for deformation sources with a range of ε that is wider than previously suggested limits. The differences between simulated surface displacements (forward modelling) and estimated deformation source parameters (inverse modelling) are less than 5% when $\varepsilon < 0.37$ (Mogi) or $\varepsilon < 0.59$ (McTigue). Misfits between analytical and FE models depend on whether radial or vertical displacements are considered simultaneously or independently, and on the values of source radius and depth - not only their ratio, as was assumed previously. There is little or no difference between best-fitting source parameters inferred using Mogi, McTigue and FE models at Kīlauea Volcano, despite the high ε of the system geometry, but sometimes poor correspondences between model results and GNSS observations. Our results demonstrate that Mogi and McTigue models can be applied to volcanoes with a wider range of magma reservoir radii and depths than was hitherto supposed, but previously-established corrections for domain simplifications are necessary to accurately interpret volcanic deformation.

1. Introduction

1.1. Volcano deformation modelling

Volcanoes deform as a response to magma migration through the subsurface. The deformation signature depends on the characteristics of magma migration and the volcano's structure (Masterlark and Tung, 2018). The properties of magma plumbing systems, particularly magma reservoirs, can therefore be inferred from deformation measurements. For example, the ratio of radial and vertical deformation fields can be used to infer magma reservoir shape (Dieterich and Decker, 1975), the rate of decay of deformation with distance is related to source depth, and the amplitude of deformation is proportional to the pressure or volume change within the source (Segall, 2019). Deformation can be recorded as ground displacements, which can be expressed in horizontal and vertical components. Ground displacements are measured using both remote sensing and ground-based techniques including Global Navigation Satellite Systems, GNSS, (e.g. Bonaccorso, 1996), interferometric synthetic aperture radar, InSAR, (e.g. Masterlark, 2007), tiltmeters (e.g. Anderson et al., 2015) and electronic distance metres, EDM, (e.g. Newman et al., 2006). Due to the inaccessibility of many volcanoes, InSAR often provides the only method of monitoring deformation (e.g. Pinel et al., 2014). By 2014, over 540 volcanoes had been studied using InSAR, many of which could not be monitored previously (Biggs et al., 2014).

Linking observed surface deformations to the inaccessible magmatic plumbing system (or other deformation sources) requires models. The displacement field is affected by properties of the magmatic plumbing system, including its location, geometry and overpressure (Masterlark and Tung, 2018). If the properties of the magmatic system are known, forward models are used to predict displacement components. Inverse modelling is required to estimate the properties of the magmatic system from observations of the displacement field.

* Corresonding author.
E-mail address: Nicola.C.Taylor@uea.ac.uk (N.C. Taylor).

https://doi.org/10.1016/j.jvolgeores.2021.107380

1.2. Numerical and analytical models

Numerical Finite Element (FE) models have been widely used for modelling volcanic systems due to their flexibility (e.g. Neuberg et al., 2018). In a FE model, the computational domain (here a deformation source embedded within a much larger half space), is discretised into many elements. The governing equations for each element are then solved, and the solution for the entire domain computed by reassembling these finite elements (Rapp, 2017). This disconnection-assembly approach allows the effects of complexities such as non-elastic rheology (e.g. Currenti et al., 2010), layering and faulting (e.g. Hickey et al., 2016) and topography (e.g. Trasatti et al., 2008) to be evaluated. Constraining these complexities typically requires data collected from the ground. For example, subsurface heterogeneities are inferred from seismic data (e.g. Masterlark et al., 2012), and anelastic rheologies from borehole temperature measurements (e.g. Castaldo et al., 2017). However, the ground-collected data required to create complex, realistic, FE models are often unavailable. Due to remoteness or inaccessibility, around 45% of volcanoes worldwide have no ground-based monitoring equipment (Pritchard et al., 2018). Furthermore, directly inverting displacement fields within FE models is typically complex, so source parameters are often first approximated using analytical models. These initial analytical results are then used within a FE model, which could incorporate heterogeneity, topography and anelastic rheology, to constrain the best fitting source (Bonaccorso et al., 2005).

Here we evaluate two simple analytical models: Mogi (Mogi, 1958) and McTigue (McTigue, 1987) against FE models. These models remain widely used for interpreting displacement fields (both in volcano geodesy and deformation modelling more generally, e.g. Liang and Dunham, 2020), as well as providing a benchmark for the calibration of FE models (e.g. Hickey and Gottsmann, 2014). The strength of Mogi and McTigue models is their remarkable ability to estimate the surface displacements and deformation source parameters, despite their computational simplicity. However, this computational simplicity comes at the expense of the assumptions that are inherent within the models; both necessitate source geometries to be embedded within elastic, homogeneous domains with a flat free surface (e.g. Pascal et al., 2014). The effect that these domain assumptions have on surface displacements can be significant, but have been described previously (e.g. Masterlark, 2007) and can often be corrected for. The high-temperature rock surrounding magma bodies has lower viscosity than the cold equivalent; incorporating viscoelasticity or temperature-dependent rheology into deformation models can significantly reduce deformation source overpressure (e.g. Hickey et al., 2013). A correction for the Mogi model to incorporate the effects of viscoelastic rheology was derived by Del Negro et al. (2009). Volcanoes are typically in areas of varying relief; steep slopes and varying source-surface separation affect the displacement field (Williams and Wadge, 1998; Cayol and Cornet, 1998) and consequently inferred source parameters (Hickey et al., 2016). Williams and Wadge (1998) describe a simple correction to account for topographic variation within analytical models, by accounting for variation in source-surface separation. Volcanic-region heterogeneity, including layering (Manconi et al., 2007), caldera ring faults (Coco et al., 2016) and weak near-surface deposits (Masterlark, 2007) can modify observed displacements. However, incorporating heterogeneity within any deformation model is often complex, because local-scale heterogeneities, which have the greatest effect on the displacement field (Masterlark, 2007), are resolved in high-resolution geophysical survey data - which are not ubiquitously available.

The difference between the Mogi and McTigue models lies in their representation of the deformation source. The Mogi model, which is the most well-known and widely-used method to compute the surface displacement components that result from a deforming magma reservoir (pressure source) (Lisowski, 2007), approximates the deformation source as a spherical anomaly, with a small radius, a, in relation to its depth, d, (i.e. a/d, ε, $\ll 1$). This small sphere source approximation necessitates $\varepsilon \ll 1$, and the limit of applicability is suggested to be $\varepsilon \lesssim 0.2$ (Lisowski, 2007), although this value has not been justified. The McTigue model extends the Mogi model by incorporating higher-order terms that account for the finite radius of a spherical deformation source. The limit of applicability of the McTigue model is suggested to be $\varepsilon = 0.5$. However, the suggested limitations for both analytical models are often ignored in practice. Whilst recognising the assumptions and simplifications in these models, their frequent use in the literature requires an objective assessment of their utility. Here we aim to investigate the limitations on ε for these analytical models by comparing them to the more sophisticated FE models, for which there is no limit on ε. The purpose of this is not to rehearse the merits of these models but to evaluate the operational limit of ε. In particular, we wish to assess their value in modelling in the face of limited field constraints.

The displacement field is differently affected by varying source radius and depth (e.g. Segall, 2019). Consequently, using ε to decide the applicability of the Mogi and McTigue models to a given situation may be an oversimplification. We thus investigate how the limit of ε is affected by varying a or d. With the aim of assessing the applicability of the models in the face of limited field data, we also investigate how the limit of ε is affected by the component of displacement that is modelled. We use forward models to test the effects of varying a, d and ε on predicted surface displacement components, and invert synthetic surface displacement components to compare the Mogi- and FE-inferred, and McTigue- and FE-inferred a and d.

We use GNSS data from two intrusion events at Kīlauea Volcano, Hawai'i, between 2007 and 2011 to demonstrate the range of ε for which FE models are statistically non-different to Mogi and McTigue models. Here, our primary aim is not to constrain the deformation source, but to demonstrate the operational applicability of simple analytical models when limited data are used. Our modelling provides guidance and limitations on the use of these simple analytical models. Our results are of particular benefit for interpreting behaviours at volcanoes where simple analytical models remain in use (for example where complex numerical models cannot be constructed due to a lack of resources or calibration data), and within the benchmarking process for FE models.

2. Methods

2.1. Forward models

We test the accuracy of the analytical models for both simulating deformation (forward modelling), and estimating source parameters (inverse modelling), whilst ε is varied by changing source radius, a, and depth d. For the forward models, we first vary ε with a. ε is increased from 0.05 to 0.70, at 0.05 intervals, whilst source depth, d, is kept constant. For each ε, the horizontal-radial, Ur, and vertical, Uz, displacement components are computed at 0.2 km intervals from $x = 0$ to $x = 25$ km using the Mogi formulae:

$$Ur = \frac{a^3 \Delta P(1-\nu)}{G} \frac{x}{R^3} \tag{1}$$

$$Uz = \frac{a^3 \Delta P(1-\nu)}{G} \frac{d}{R^3} \tag{2}$$

and the McTigue formulae:

$$Ur = \frac{a^3 \Delta P(1-\nu)x}{GR^3}\left(1 + \left(\frac{a}{d}\right)^3\left(\frac{1+\nu}{2(-7+5\nu)} + \frac{15d^2(-2+\nu)}{4R^2(-7+5\nu)}\right)\right) \tag{3}$$

$$Uz = \frac{a^3 \Delta P(1-\nu)d}{GR^3}\left(1 + \left(\frac{a}{d}\right)^3\left(\frac{1+\nu}{2(-7+5\nu)} + \frac{15d^2(-2+\nu)}{4R^2(-7+5\nu)}\right)\right) \tag{4}$$

where $R = (x^2 + d^2)^{0.5}$, ΔP is source overpressure, ν Poisson's ratio and G shear modulus. Surface displacements may alternatively be

formulated in terms of a volume change (e.g. magma injection into, or withdrawal from, a magma reservoir), requiring additional terms that describe magma compressibility (Delaney and McTigue, 1994; Johnson et al., 2000). We maintain constant source overpressure ($\Delta P = 2$ MPa), and note that deformation scales linearly with overpressure for analytical and numerical models (Fig. S1). We extract the maximal horizontal-radial and vertical displacement components, Ur_{max} and Uz_{max}, and the distance to Ur_{max}, x_{crit}, for each ε. We also compute the second derivative of Ur, Ur'', and of Uz, Uz'', to find the inflection points, $x(Ur'' = 0)$ and $x(Uz'' = 0)$, a measure of displacement profile shape. This is repeated for five depths (1, 4, 7, 10 and 13 km). These depths, and other model parameters (see Table 1) are based on Kīlauea Volcano, a Hawaiian basaltic shield volcano, but the results are applicable elsewhere. We vary ε with d following the same procedure as for varying a. Ur, Ur'', Ur_{max}, x_{crit}, Uz, Uz'' and Uz_{max} are computed using the analytical Mogi and McTigue formulae. ε is increased from 0.05 to 0.70, whilst source radius, a, is kept constant. The procedure is repeated for a = 0.5, 1.5, 2.5, 3.5 and 4.5 km. We do not process results for combinations of ε and a where d exceeds 30 km, because most magma reservoirs are shallower than this (e.g. Edmonds et al., 2019).

We compare the analytical results to those obtained numerically using FE models. COMSOL Multiphyiscs® (v5.4) is used for FE modelling. We use a 2D-axisymmetric model within the stationary structural mechanics module. A spherical cavity is embedded within an elastic, homogeneous half-space, with a flat free surface. This simple geometry is chosen to allow the best comparison between FE and analytical models, even though FE modelling allows additional complexities. The overpressure, ΔP, is applied uniformly to the cavity walls. The domain is substantially larger than the source, and surrounded by an infinite element domain such that boundary effects are insignificant. Model configuration is shown in Fig. 1 and model parameters in Table 1. A triangular mesh is used, with a minimum dimension of 10 m (Fig. S2, Table S1). The FE model is benchmarked against Mogi and McTigue models for low ε (Fig. S3). Our FE models are run with the same values of a, d, and ε as used within analytical models; a is varied for ε between 0.05 and 0.70, whilst d is kept constant (with five depths, 1, 4, 7, 10 and 13 km tested for each ε), then d is varied for ε between 0.05 and 0.70, whilst a is kept constant (with five radii, 0.5, 1.5, 2.5, 3.5 and 4.5 km tested for each ε). Ur and Uz are exported at 0.2 km intervals from $x = 0$ to $x = 25$ km, and Ur_{max}, x_{crit}, Uz_{max}, $x(Ur'' = 0)$ and $x(Uz'' = 0)$ are calculated. For all tested ε, we compute the differences in Mogi- and FE-derived, and McTigue- and FE-derived maximal displacement components, ΔUr_{max} and ΔUz_{max}, and in displacement profile inflection points, $\Delta x(Ur'' = 0)$ and $\Delta x(Uz'' = 0)$. We compute the median differences in Ur and Uz, ΔUr and ΔUz, for x between 0 and $3x_{crit}$. For some combinations of source parameters, displacement over most of the domain is negligible. Applying a limit on x ensures that differences in Ur and Uz are predominantly computed over regions of observable displacement.

Table 1
Parameters used within Mogi, McTigue and FE models to compute deformation (forward models) and infer source properties (inverse models).

	Symbol	Definition	Units	Value
Domain parameters	G	Shear modulus	GPa	4.0
	ν	Poisson's ratio	–	0.25
Source parameters	ΔP	Overpressure	MPa	2.0
	a	Radius	km	Model variable
	d	Depth	km	Model variable
	ε	a/d	–	0.05 − 0.70
Results	Ur	Horizontal-radial deformation	m	Result
	Uz	Vertical deformation	m	Result
	Ur_{max}	Maximum horizontal-radial deformation	m	Result
	Uz_{max}	Maximum vertical deformation	m	Result

The domain is homogeneous, elastic and has a flat free surface and all sources are spherical. Fixed parameters (domain parameters and source overpressure) are based on Kīlauea Volcano, Hawai'i, a basaltic shield volcano. Source radius is varied for ε between 0.05 and 0.70, with depths of 1, 4, 7, 10 and 13 km and source depth is varied for ε between 0.05 and 0.70, with radii of 0.5, 1.5, 2.5, 3.5 and 4.5 km.

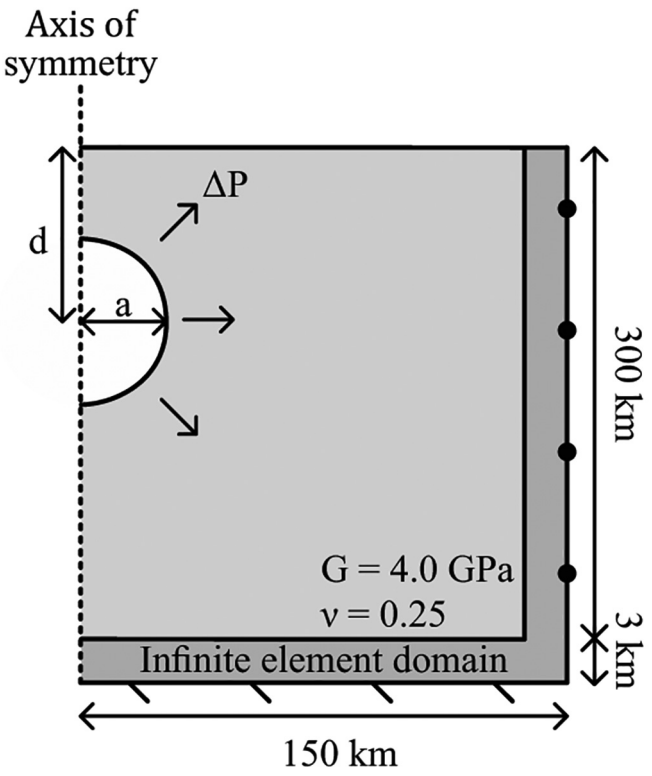

Fig. 1. Finite Element model configuration. Using a 2D axisymmetric model domain, a spherical cavity with radius a, at depth d, is embedded within an elastic, homogenous domain with a flat free surface. A constant overpressure, ΔP, is applied to the cavity walls. The domain is significantly larger than the cavity and is surrounded by an infinite element domain, to reduce boundary effects. The top surface is free, the bottom surface is fixed and a roller condition is applied to prevent displacements perpendicular to the right boundary. The domain is described by its shear modulus, G and Poisson's ratio, ν. A triangular mesh is used throughout the model. The mesh elements in the upper 4 km of the model have a maximum size of 0.01 km. Elsewhere in the domain, mesh elements have sizes between 0.09 and 20.3 km, finest near the source. Further details about the mesh in Fig. S2. Not to scale.

2.2. Inverse models

For inverse modelling, we compare a and d inferred from Mogi and FE models, and McTigue and FE models. Considering first ε varying with a (for each of the five depths tested). For each previously-tested value of ε, we use linear parameter estimation to invert FE-derived Ur_{max}, then Uz_{max}, to seek solutions for a within the Mogi framework:

$$a^3 = \frac{GUr_{max}}{\Delta P(1-\nu)}\frac{R^3}{x_{crit}} \tag{5}$$

$$a^3 = \frac{GUz_{max}}{\Delta P(1-\nu)}\frac{R^3}{d} \tag{6}$$

and McTigue framework:

$$\rho_r = Ur_{max} - \frac{a^3\Delta P(1-\nu)x}{GR^3}\left(1 + \left(\frac{a}{d}\right)^3\left(\frac{1+\nu}{2(-7+5\nu)} + \frac{15d^2(-2+\nu)}{4R^2(-7+5\nu)}\right)\right) \tag{7}$$

$$\rho_z = Uz_{max} - \frac{a^3\Delta P(1-\nu)d}{GR^3}\left(1+\left(\frac{a}{d}\right)^3\left(\frac{1+\nu}{2(-7+5\nu)}+\frac{15d^2(-2+\nu)}{4R^2(-7+5\nu)}\right)\right) \quad (8)$$

For the McTigue framework, we solve for a by minimising the residuals ρ_r and ρ_z associated with the radial or vertical components of displacement respectively. We then use linear parameter estimation (e.g. Gubbins, 2004) to invert FE-derived Ur_{max} and Uz_{max} simultaneously within Mogi (Eq. (9)) and McTigue (Eq. (10)) frameworks, seeking solutions for a that minimise the sum of squared residuals ρ_r and ρ_z (i.e. $\rho_r^2 + \rho_z^2$):

$$\begin{bmatrix} Ur_{max} \\ Uz_{max} \end{bmatrix} = a^3 \begin{bmatrix} \frac{\Delta P(1-\nu)}{G}\frac{x}{R^3} \\ \frac{\Delta P(1-\nu)}{G}\frac{d}{R^3} \end{bmatrix} + \begin{bmatrix} \rho_r \\ \rho_z \end{bmatrix} \quad (9)$$

$$\begin{bmatrix} Ur_{max} \\ Uz_{max} \end{bmatrix} = \begin{bmatrix} \frac{a^3\Delta P(1-\nu)x}{GR^3}\left(1+\left(\frac{a}{d}\right)^3\left(\frac{1+\nu}{2(-7+5\nu)}+\frac{15d^2(-2+\nu)}{4R^2(-7+5\nu)}\right)\right) \\ \frac{a^3\Delta P(1-\nu)d}{GR^3}\left(1+\left(\frac{a}{d}\right)^3\left(\frac{1+\nu}{2(-7+5\nu)}+\frac{15d^2(-2+\nu)}{4R^2(-7+5\nu)}\right)\right) \end{bmatrix} + \begin{bmatrix} \rho_r \\ \rho_z \end{bmatrix} \quad (10)$$

This procedure is repeated for ε varying with d, whilst a is constant (as for forward models, five source radii are tested). Considering Ur_{max} and Uz_{max} independently, the Mogi equations are rearranged (Eqs. (11), (12)) to solve for d for all ε:

$$d^2 = \left(\frac{a^3\Delta P(1-\nu)x_{crit}}{GUr_{max}}\right)^{2/3} - x_{crit}^2 \quad (11)$$

$$d^2 = \frac{a^3\Delta P(1-\nu)}{GUz_{max}} \quad (12)$$

For the McTigue model, we seek solutions for d that minimise ρ_r and ρ_z within Eqs. (7) and (8). For the simultaneous inversion of Ur_{max} and Uz_{max} within the Mogi framework, Eq. (13) is used to seek solutions for d that minimise the sum of squared residuals ρ_r and ρ_z. For the McTigue scenario, Eq. (10) is solved for d, again minimising the sum of the squared residuals.

$$\begin{bmatrix} Ur_{max} \\ Uz_{max} \end{bmatrix} = d^2 \begin{bmatrix} \left(\frac{a^3\Delta P(1-\nu)x_{crit}}{GUr_{max}}\right)^{2/3} - x_{crit}^2 \\ \frac{a^3\Delta P(1-\nu)}{GUz_{max}} \end{bmatrix} + \begin{bmatrix} \rho_r \\ \rho_z \end{bmatrix} \quad (13)$$

We compute the differences in Mogi- and FE-inferred, and McTigue- and FE-inferred radius, Δa, and depth, Δd. We use Mogi and McTigue models to compute the surface displacement components that sources with these inferred geometries produce, and compare these to the surface displacement components predicted by FE models.

3. Results

3.1. Forward models

As ε increased with a, analytical models increasingly underestimated maximal displacement components, Ur_{max} and Uz_{max} (Fig. 2 upper plots; Ur_{max} and Uz_{max} values in Fig. S4). Analytical models also increasingly underestimated Ur_{max} and Uz_{max} as ε increased with decreasing d (Fig. 2, lower plots). For all ε, the correspondence between McTigue and FE models was greater than for Mogi and FE models.

The percentage misfits between analytical and FE-derived Ur_{max} (ΔUr_{max}) and Uz_{max} (ΔUz_{max}), relative to ε, are analysed using using nonlinear least squares regression - fitted curves are of the form $\Delta U_{max} = A^{B\varepsilon}$ where ΔU_{max} is ΔUr_{max} or ΔUz_{max} and A and B are constants (all statistical analyses conducted R v.4.0.2.; packages *stats*, *dunn.test*). ΔUr_{max} and ΔUz_{max} depend on ε, rather than the values of a or d, for ε varying with both a and d. We define ε_c as ε where the misfit between analytical and FE model solutions is 5%: $\varepsilon(\Delta Ur_{max} = 5\%)$ or $\varepsilon(\Delta Uz_{max} = 5\%)$ (Fig. 3a). Table 2 summarises these results. Kruskal-Wallis tests were used to consider whether differences in ε_c were significant at a 95% confidence level. Critical p-values were adjusted for multiple comparisons (Fig. S5 and Table S2 for full statistical results). ε_c was greater for McTigue models than for Mogi models ($p < 0.001$, $n = 20$). For both analytical models, ε_c when Ur_{max} was predicted was significantly greater than when Uz_{max} was predicted ($p < 0.001$, $n = 10$), but ε_c did not depend on whether ε varied with a or d.

We plot the median difference in Ur, ΔUr, and the median difference in Uz, ΔUz, for ε varying with a and d (Fig. 4). For both analytical models, ΔUr and ΔUz increased with ε. For McTigue models ΔUr and ΔUz remained small (below 3%) for all tested ε. When ε increased with a, the increase in ΔUr and ΔUz was greater than when ε varied with d. The ratio of a to d typically has a greater effect on ΔUr and ΔUz than the values of a and d.

Fig. 5 displays the differences in inflection points for radial and vertical displacement profiles, $x(Ur'' = 0)$ and $x(Uz'' = 0)$. As ε increased with a, FE models predicted that the distance to the displacement profile inflection point decreased. This was not predicted by Mogi models, and the decrease in distance to $x(Ur'' = 0)$ and $x(Uz'' = 0)$ for increasing ε is underestimated by McTigue models. When ε increased with decreasing d, both analytical and FE models predicted that $x(Ur'' = 0)$ and $x(Uz'' = 0)$ decreased, but for larger ε, Mogi and McTigue models underestimated this decrease.

3.2. Inverse models

As ε increased, the difference between Mogi- and FE-inferred, and McTigue- and FE-inferred radius, Δa, and depth, Δd, increased (Fig. 6, Fig. S6 for inferred radii and depths). Δa and Δd were consistently greater for Mogi than for McTigue models, and for both analytical models Δa and Δd increase more rapidly with ε for the inversion of Uz_{max} compared to Ur_{max}.

Nonlinear least squares regression was used to relate Δa and Δd to ε and compute ε_c, $\varepsilon(\Delta a = 5\%)$ or $\varepsilon(\Delta d = 5\%)$ (Fig. 3b). Again, regression curves were of the form Δa or $\Delta d = A^{B\varepsilon}$ where A and B are constants. Differences in ε_c for Mogi and McTigue simulations were assessed using Kruskal-Wallis tests and post-hoc Dunn's tests where appropriate (Fig. S5 and Table S2). As for the forward models, ε_c for McTigue models was significantly greater than for Mogi models ($p < 0.001$, $n = 30$). For both analytical models, ε_c was greater for the inversion of Ur_{max} than of Uz_{max} or total displacement ($p < 0.001$, $n = 10$). ε_c was also greater for both Mogi and McTigue models when a was estimated than when d was estimated ($p = 0.0095$ and $p = 0.0026$ for Mogi and McTigue models respectively, Bonferroni-adjusted critical $p = 0.01$, $n = 15$).

We plot the median differences in Mogi- and FE-derived, and McTigue- and FE-derived Ur, ΔUr, and Uz, ΔUz, for sources with radii and depths inferred using Mogi and McTigue models (Fig. 7). Analogous to the forward models, ΔUr and ΔUz increase with ε and are consistently greater for Mogi models than for McTigue models. ΔUr and ΔUz are also greater for ε varying with a than with d, particularly for McTigue models.

4. Discussion

The Mogi model (Mogi, 1958), has been extensively used to interpret ground deformation data resulting from magma movement (e.g.

Amelung et al., 2000), as well as from ground water and hydrothermal fluid extraction (Carnec and Fabriol, 1999; Liu et al., 2016). The model makes assumptions about the embedding domain - it is elastic, homogeneous and has a flat free surface - and about the source, which has a small radius to depth ratio (a/d, ε, $\ll 1$). The effect that the domain simplifications have on the surface displacement field have been previously assessed (e.g. Masterlark, 2007), and corrections for these can be applied (e.g. Williams and Wadge, 1998; Del Negro et al., 2009). However, the limit of ε for applying the Mogi model has not been validated (e.g. Lisowski, 2007). The McTigue model (McTigue, 1987) offers an improvement on the Mogi model, for relatively little additional computational cost. Using the same assumptions of a homogenous, elastic domain, with a flat free surface, McTigue accounted for the finite dimensions of a spherical source in order to predict volcanic deformation and infer source parameters with greater accuracy.

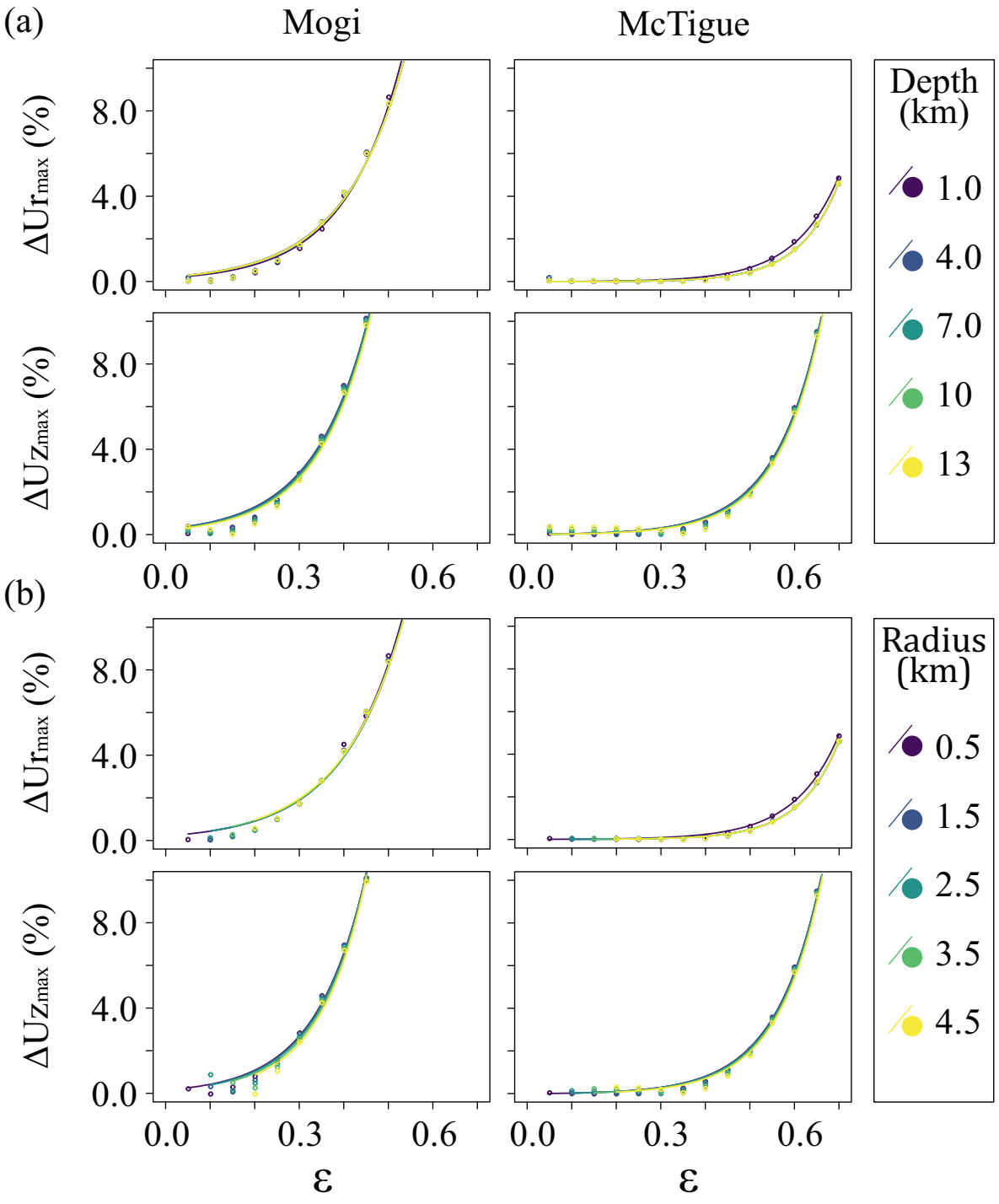

Fig. 2. Effects of varying source radius and depth on deformation. The percentage difference between Mogi and FE (left column) and McTigue and FE (right column) horizontal-radial (ΔUr_{max}) and vertical (ΔUz_{max}) displacements increases with ε, for ε varying with radius (a) and depth (b). Nonlinear least-squares regressions are drawn. ΔUr_{max} and ΔUz_{max} depend on the ratio of radius and depth. Fig. S4 plots Ur_{max} and Uz_{max}.

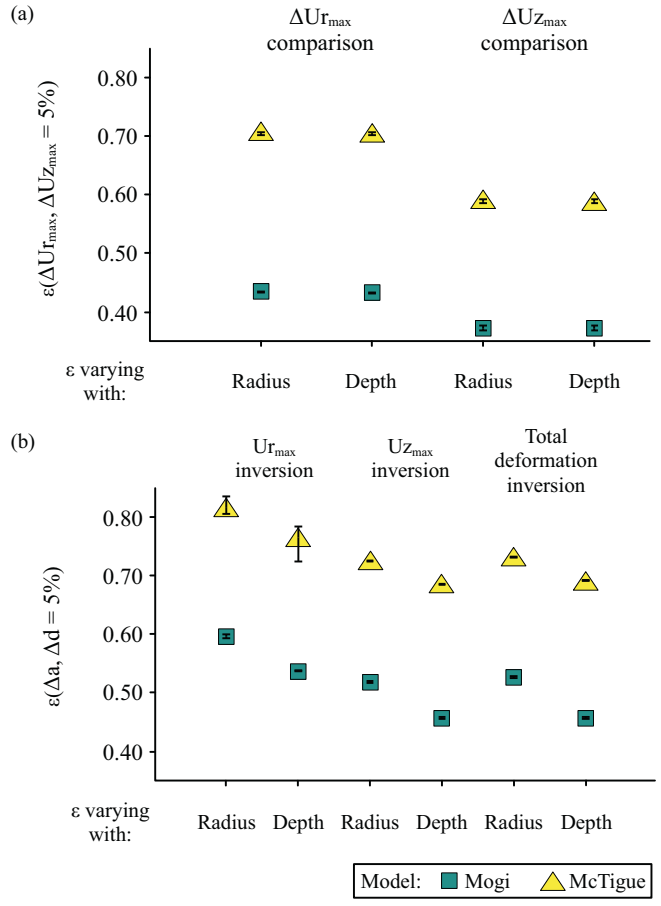

Fig. 3. Correspondence between Mogi and FE, and McTigue and FE models. (a) Results for forward models, ε_c defined where the difference between modelled maximal horizontal-radial (ΔUr_{max}) or vertical (ΔUz_{max}) displacements is 5%. (b) Results for inverse models, ε_c defined where the difference between modelled source radius (Δa) or depth (Δd) is 5%. ε_c are calculated using non-linear regression, $\varepsilon_c > 0.70$ should be interpreted with caution, because regressions have been extended beyond the limits of our models (tested $\varepsilon \leq 0.7$). Error bars show the range of results ($n = 5$ for each point).

We compared surface displacement components predicted by, and source properties inferred from, Mogi and FE models, and McTigue and FE models to validate the range of ε for which the Mogi and McTigue models should be applied. We set the critical threshold for difference between analytical and FE models to 5%. This is acceptable because the uncertainties that arise from volcano modelling are inherently large. Volcanoes are natural systems that are intrinsically unpredictable because they display stochastic, highly nonlinear behaviors - all volcanic systems must be simplified to make a model tractable (Sparks, 2003). Further uncertainty is introduced with monitoring data, which are collected from instruments that have finite accuracy, often within temporally and/or spatially sparse instrumental arrays. Consequently, model results often span a large range (e.g. Becerril et al., 2013), or are associated with a probability density function (e.g. Anderson and Segall, 2011).

4.1. Finite body effects

We found agreement between Mogi and FE models for a wider range of ε than previously assumed. Our forward model results showed that Mogi- and FE-derived Ur_{max} and Uz_{max} were within 5% when $\varepsilon < 0.37$. For inverse models, we found that Mogi- and FE-inferred a and d were within 5% when $\varepsilon < 0.46$. For ε below these values, finite body effects are negligible. Thus, both forward and inverse model results suggest that, for interpreting surface displacement fields, limiting Mogi model application to $a \ll d$, or $a/d \ll 1$ is unnecessary. The McTigue model makes a higher-order correction for these finite body effects, therefore this model shows better correspondence with FE models for larger ε. McTigue- and FE-derived Ur_{max} and Uz_{max} were within 5% when $\varepsilon < 0.59$ and McTigue- and FE-inferred a and d were within 5% when $\varepsilon < 0.69$. McTigue (1987) demonstrated analytically that the effect of a finite body on surface uplift is often small, a conclusion that our numerical results support. Hence we have more confidence in the results of Mogi modelling at volcanoes where $\varepsilon \not\ll 1$, including at Soufrière Hills, Montserrat ($\varepsilon \lesssim 0.46$),(Widiwijayanti, 2005).

4.2. Non-unique ε_c

Although we found that the Mogi model could be applied for a wider range of ε than previously assumed, we did not obtain a unique value for ε_c (Fig. 3). The mean ε_c, at which the misfit between Mogi and FE solutions was 5%, was greater for inverse models than for forward models. For the comparison between McTigue and FE models, ε_c was also greater for inverse than for forward models. We therefore have more confidence using analytical models to invert displacement fields to estimate deformation source parameters, than we do predicting the displacement field from an already-known source, particularly when a $\not\ll$ d. Inverse modelling is used to correlate the observed displacement field with source characteristics (Amelung et al., 2000), and

Table 2
Critical ε, ε_c, computed from forward and inverse modelling.

	Forward models		Inverse models	
	Estimate	ε_c	Invert	ε_c
Mogi: Varying a	Ur_{max}	0.434 ± 0.001	Ur_{max}	0.597 ± 0.004
	Uz_{max}	0.371 ± 0.006	Uz_{max}	0.519 ± 0.003
			Ur_{max} and Uz_{max}	0.526 ± 0.003
McTigue: Varying a	Ur_{max}	0.705 ± 0.004*	Ur_{max}	0.817 ± 0.020*
	Uz_{max}	0.588 ± 0.004	Uz_{max}	0.726 ± 0.0001*
			Ur_{max} and Uz_{max}	0.732 ± 0.001*
Mogi: Varying d	Ur_{max}	0.432 ± 0.002	Ur_{max}	0.538 ± 0.001
	Uz_{max}	0.371 ± 0.006	Uz_{max}	0.457 ± 0.002
			Ur_{max} and Uz_{max}	0.457 ± 0.002
McTigue: Varying d	Ur_{max}	0.705 ± 0.004*	Ur_{max}	0.765 ± 0.042*
	Uz_{max}	0.588 ± 0.004*	Uz_{max}	0.686 ± 0.001*
			Ur_{max} and Uz_{max}	0.692 ± 0.001

For forward models, $\varepsilon_c = \varepsilon(\Delta Ur_{max} = 5\%)$ or $\varepsilon(\Delta Uz_{max} = 5\%)$. For inverse models, $\varepsilon_c = \varepsilon(\Delta a = 5\%)$ or $\varepsilon(\Delta d = 5\%)$. All ε_c are found using non-linear regression, using the mean values for the 5 depths (ε varying with a) or 5 radii (ε varying with d) and the uncertainty is twice the standard deviation. Only $\varepsilon \leq 0.7$ were tested; linear regressions have been interpolated beyond the model results to obtain some ε_c, denoted by * - these results should be interpreted with caution.

* Interpolated result.

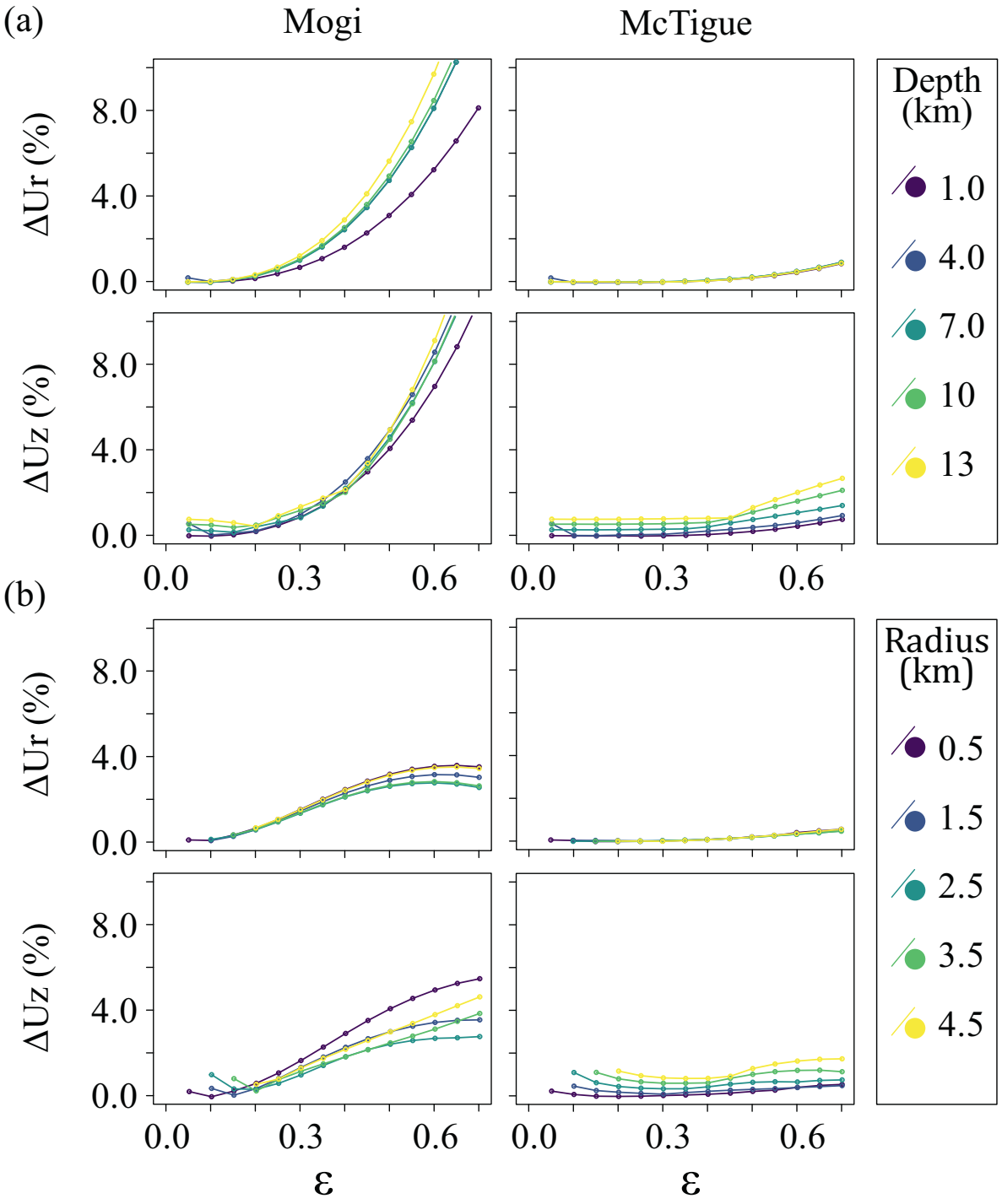

Fig. 4. Increase in median difference between Mogi and FE, and McTigue and FE, horizontal-radial (ΔUr) and vertical (ΔUz) displacements with ε. (a) ε varying with source radius and (b) ε varying with source depth. Discrepancies between analytical and numerical results for ΔUr and ΔUz at small ε are attributed to the finite size of the mesh. For vertical displacements, the difference between analytical and numerical models is of the order 10^{-7}m (Fig. S3) whereas the smallest ΔUr and ΔUz are of the order 10^{-8}m. However, these differences are insignificant because displacements of this magnitude cannot be detected by monitoring instruments.

even when FE models are subsequently used, analytical models are often used to compute a first approximation of source parameters (e.g. Bonaccorso et al., 2005). Thus obtaining a greater ε_c for inverse models is a useful outcome.

ε_c varied between forward and inverse models, but also depended on the component of displacement that was simulated (forward models) or inverted (inverse models) (Fig. 3). For forward models, ε_c was significantly greater for estimating Ur_{max} than Uz_{max} ($p < 0.001$ for both Mogi and McTigue comparisons), and for inverse models, ε_c was significantly greater for inverting Ur_{max}, compared to Uz_{max} ($p < 0.001$ for both Mogi and McTigue comparisons). These results suggest that it should preferable to invert horizontal-radial displacements within analytical models, contrary to previous studies which inverted the vertical components of GNSS (e.g. Puglisi and Bonforte, 2004) or InSAR (e.g. Tiampo et al., 2017) measurements. However, accurate radial displacement data are not ubiquitously available.

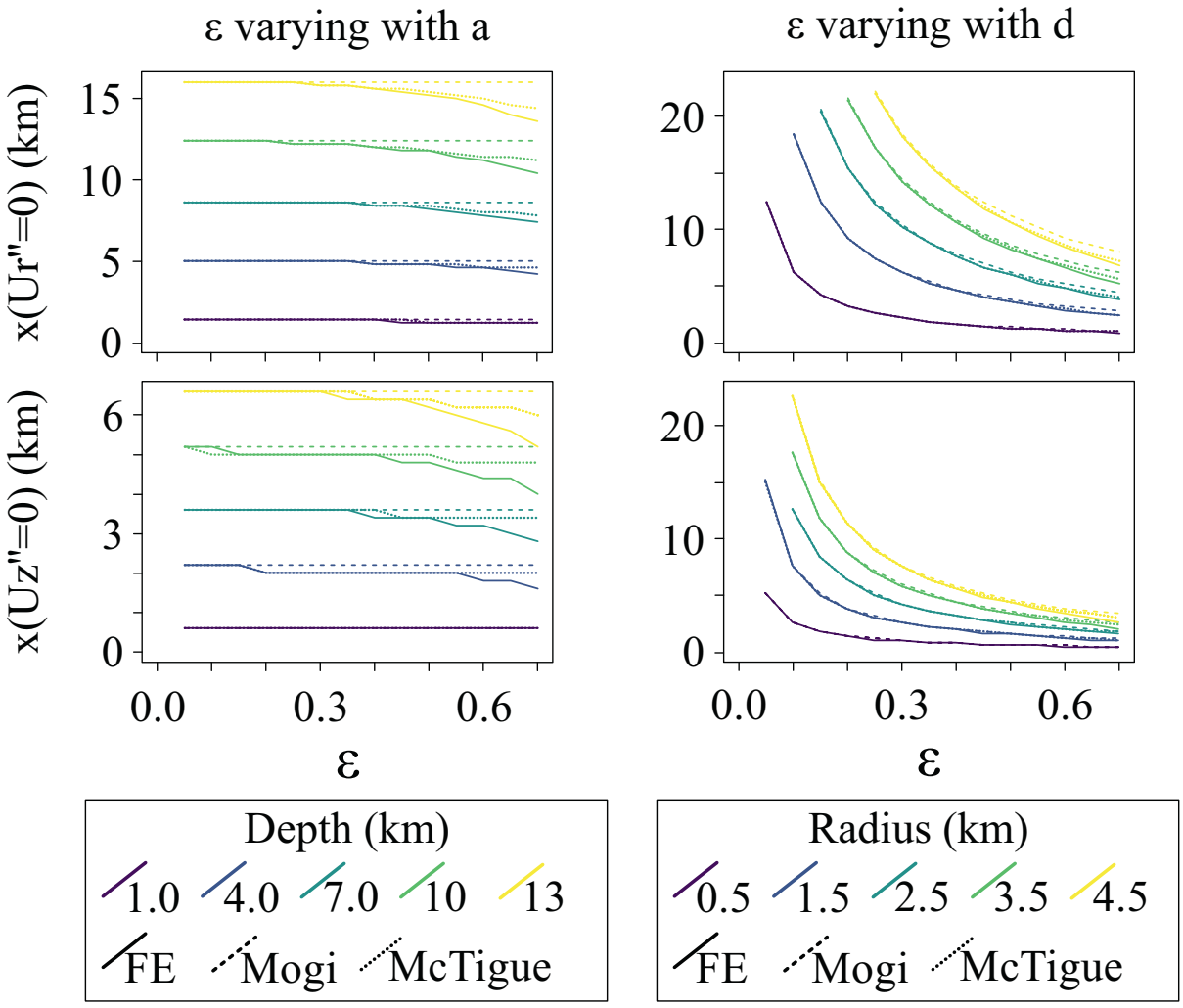

Fig. 5. Effect of ε on deformation profile width. Deformation profile width is quantified using the inflection points of horizontal-radial, $x(Ur'' = 0)$, and vertical, $x(Uz'' = 0)$, displacement profiles.

Analytical models are particularly useful for interpreting InSAR data from remote, inaccessible volcanoes where ground-based sensors cannot be deployed, and the calibration data required for more complex, realistic numerical models cannot be collected. Unfortunately, the horizontal displacements that are calculated from InSAR line-of-sight displacements are associated with large uncertainty, particularly in the North-South direction (Henderson and Pritchard, 2017). However, where GNSS stations can be deployed, the uncertainty of these data is greater in the vertical direction (Eckl et al., 2001). Thus, although the analytical-FE model correspondence is better for a wider range of ε when the horizontal-radial component of the deformation field is evaluated, when InSAR data are being considered it is likely that evaluating the vertical deformation field is preferable.

The correspondence between analytical and FE models also depended on whether ε was varied with a or d. For forward models, ε_c did not depend on whether ε varied with a or d. This aligns with previous assumptions (e.g. Lisowski, 2007) that it is the ratio of a and d (i.e. ε), rather than the values of a and d that dictates the applicability of Mogi or McTigue models (Fig. 3). However, when ε increased with a, ΔUr and ΔUz increased quasi-exponentially, whereas when ε increased with d, the rate of increase of ΔUr and ΔUz was smaller, and often plateaued. The increases in ΔUr and ΔUz for ε increasing with a are attributed to the analytical models underestimating (McTigue model), or not reproducing (Mogi model), the change in displacement profile width (computed using inflection points, Fig. 5) predicted by FE models. When ε increased with d, the change in displacement profile width was predicted, but underestimated, by both analytical models. For inverse models, for both Mogi and McTigue comparisons, ε_c was greater for estimating a than for estimating d. Yet ΔUr and ΔUz were smaller for ε varying with d than with a. The inversions from which ε_c were calculated only used maximal horizontal-radial and/or vertical displacements. If more displacement data were used, our results suggest that ε_c would be greater for ε varying with d than with a, because the overall correspondence across a displacement profile is greater for sources with small d than with large a (for the same ε). Thus, for both forward and inverse models, we suggest that Mogi and McTigue models perform better when the deformation source a/d ratio is increased with small d than with large a.

4.3. Limitations

We found good agreement between Mogi, McTigue and FE models for a wider range of ε than was previously assumed. As expected, there is good correspondence between McTigue and FE models for a wider range of ε than for Mogi and FE models. However, both Mogi and McTigue models are based on numerous other simplifications that affect their applicability for interpreting the surface displacement field (e.g. Masterlark, 2007). Like all volcano models, Mogi and McTigue

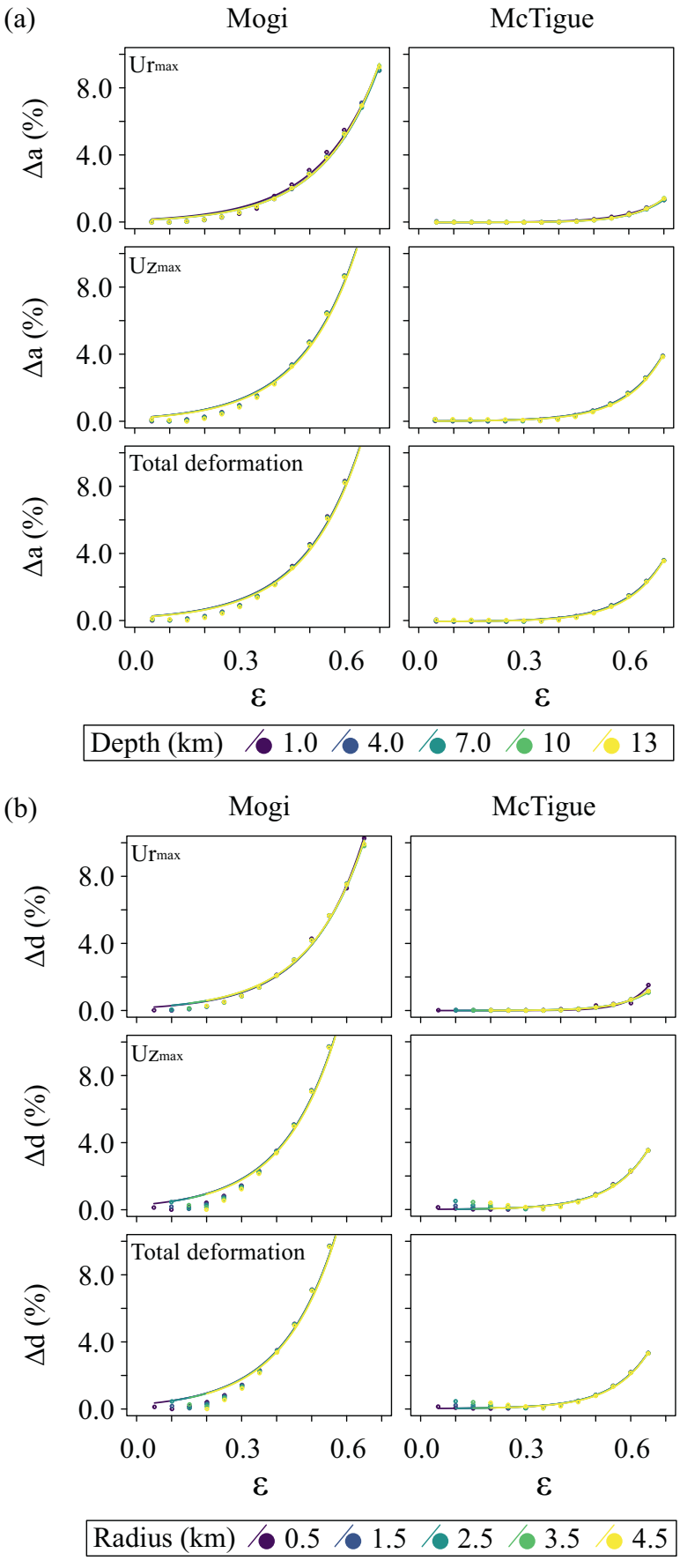

Fig. 6. Correspondence between source radii and depths inferred using Mogi and FE, and McTigue and FE models. Differences in (a) inferred source radii, Δa, and (b) inferred source depths, Δd, are evaluated by inverting maximal horizontal-radial, Ur_{max}, and vertical, Uz_{max}, components of displacement independently and simultaneously. Fig. S6 displays inferred values of a and d.

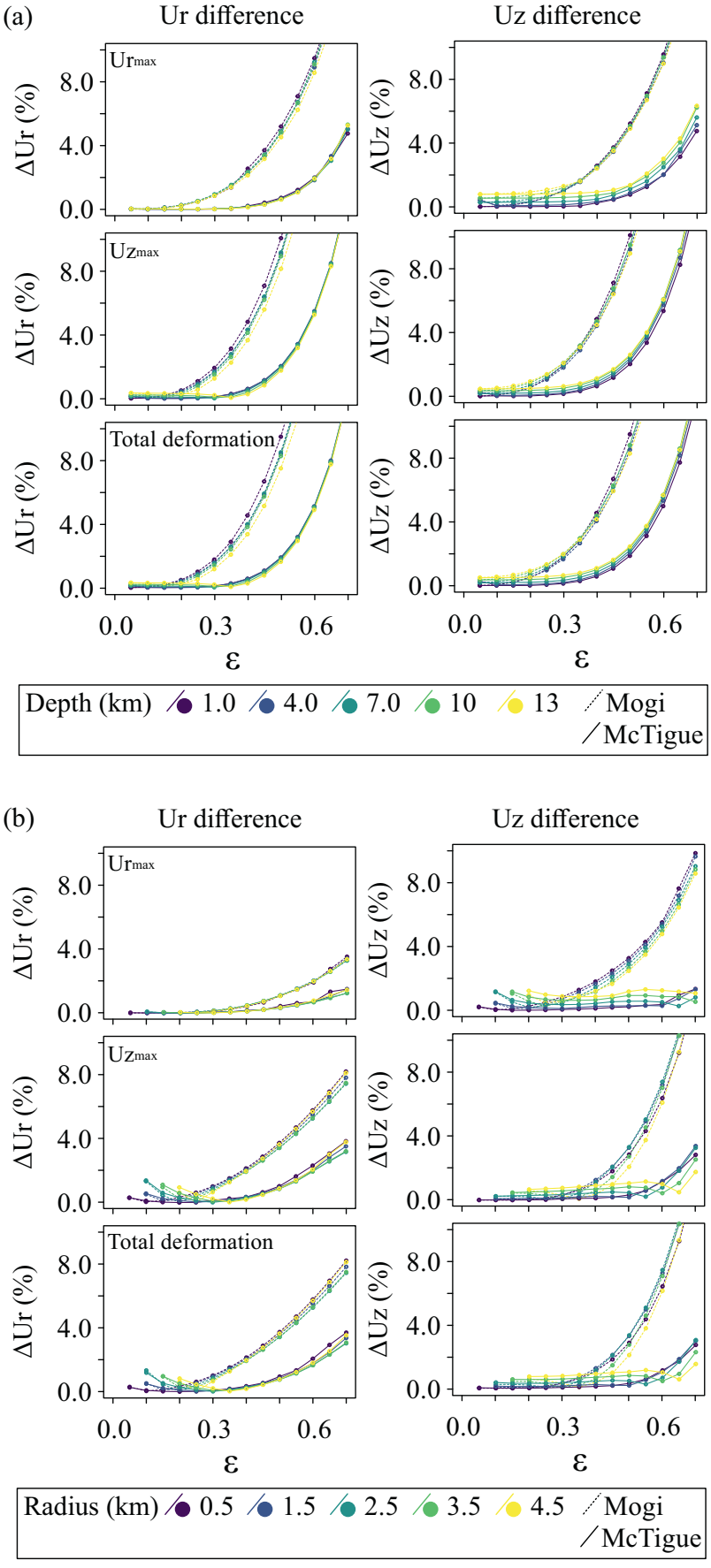

Fig. 7. Variation between analytically- and numerically-derived displacement profiles from inverse models. Median differences in horizontal-radial, ΔUr, and vertical, ΔUz, displacement components plotted for (a) analytically-inferred source radius varied with ε and (b) analytically-inferred source depth varied with ε. Differences in ΔUr and ΔUz for small ε attributed to the error between analytical and FE models (Fig. S3) due to the finite size of the mesh, they are of the order 10^{-8}m.

models necessarily simplify complex, often poorly understood, volcanic systems to allow natural phenomena to be explained quantitatively. Simulating a magma reservoir as either a small spherical (Mogi) or finite spherical (McTigue) anomaly is incorrect; magma reservoirs comprise mush and rock, melt exists within finite regions inside a crystalline framework, alongside exsolved magmatic fluids (Edmonds et al., 2019). The shape of this region is likely to be irregular and non-spherical. Altering the shape of the magma reservoir alters the deformation pattern (e.g. Currenti, 2018). In addition, magma reservoirs are not embedded in homogeneous elastic domains. The high temperatures of magma bodies reduce the viscosity of surrounding rock by several orders of magnitude (Segall, 2019), and introducing viscoelasticity into a model affects the pattern and magnitude of deformation (e.g. Currenti et al., 2010; Head et al., 2019). Volcanic regions often comprise layered deposits with substantially different stiffnesses (e.g. Hickey et al., 2017); heterogeneity can amplify or mute displacement vectors (e.g. Manconi et al., 2007; Geyer and Gottsmann, 2010), and affects the ratio of horizontal to vertical displacement components (Hautmann et al., 2010). In addition, topography around volcanoes is rarely flat, and slopes or cliffs affect deformation (e.g. Cayol and Cornet, 1998; Hickey et al., 2016; Johnson et al., 2019). It is also unlikely that source pressurisation remains constant.

Despite these limitations, the simple Mogi and McTigue models have performed well within volcano geodesy, and remain well-used to interpret deformation (e.g. Liang and Dunham, 2020). We show that the applicability of the Mogi model, relating to ε, is likely to be greater than previously assumed, because of its correspondence with FE results when $\varepsilon \not\ll 1$. We also show that the applicability of the McTigue model is greater than previously assumed. For magma reservoirs there is a limit on ε that is imposed by the strength of the overlying country rock. Exceeding this limit results in tensile fracture (e.g. Grosfils, 2007; Zhan et al., 2017). Quantifying this limit is beyond the scope of this paper, but we suggest that it is likely that there are few, if any, magma reservoirs with dimensions outside of the range that can be described by McTigue models. However, due to the numerous other assumptions that the Mogi and McTigue models make, these models are best used to provide a first-order estimate of deformation source parameters. For some scenarios, particularly at remote volcanoes, this may be all that is required.

4.4. Kīlauea modelling: background

Kīlauea Volcano is a basaltic shield volcano on the island of Hawai'i. Volcanism along the Hawaiian-Emperor chain of seamounts and islands, which includes Hawai'i, is attributed to the Hawaiian hotspot, Earth's most productive mantle-melting anomaly (Poland et al., 2014). Kīlauea is one of the best monitored volcanoes on Earth (e.g. Garcia, 2015), and geodetic, seismic and petrologic data have been used to constrain the magmatic plumbing system at Kīlauea (e.g. Edmonds et al., 2013; Lin et al., 2014; Poland and Carbone, 2016). This plumbing system includes two magma reservoirs beneath Kīlauea's summit, the South Caldera Reservoir at around 3 − 4 km depth, and the smaller Halema'uma'u Reservoir at around 1 − 2 km depth (Poland et al., 2014). There has been a direct connection between Halema'uma'u Reservoir and Kīlauea's summit. Between 2010 and 2018 there was an almost-continuously active lava lake at the summit (Patrick et al., 2016). This lava lake was directly connected to the Halema'uma'u Reservoir through an open vent (e.g. Patrick et al., 2019).

Kīlauea's East and Southwest Rift Zones (ERZ and SWRZ respectively) are connected to the South Caldera Reservoir via conduits at around 3 km depth (Poland et al., 2014). Volcanic activity within the ERZ was continuous between 1983 and 2018 (Orr et al., 2015). Here we model two events during this period: the June 2007 'Father's day' event and the March 2011 Kamoamoa Fissure Eruption. These two events were associated with significant deflation at Kīlauea's summit, which is clearly seen in GNSS data. The deflation was caused by a drop in Halema'uma'u Reservoir pressure (and associated drop in lava lake level) as magma drained into the ERZ (Lundgren et al., 2013; Orr et al., 2015). The magnitude of the pressure change within Halema'uma'u Reservoir can be calculated using tilt data from Kīlauea's summit (Patrick et al., 2015).

Previous studies, including Johnson et al. (2010); Baker and Amelung (2012); Chouet and Matoza (2013); Edmonds et al. (2013); Anderson et al. (2015), have used a range of geodetic, geophysical and geochemical datasets from intrusive events to accurately constrain the properties and location of the Halema'uma'u Reservoir. We take a different approach by comparing the geometry (radius and depth) of the Halema'uma'u Reservoir that is inferred when the same data (GNSS-derived deformations) are used within Mogi, McTigue and FE models, thereby extending the analyses described earlier in this manuscript where only synthetic deformation data were considered. All three of these models have been widely used to infer magma reservoir properties at both at Kīlauea and volcanoes elsewhere, but to date there has been no direct comparison of the deformation source properties inferred using these models, nor of the limits of applicability of the two analytical models.

4.5. Kīlauea modelling: method

Twenty one days of GNSS measurements were analysed for each intrusion event (data in Table S6). Data from two GNSS stations (BYRL and UWEV) were considered for the June 2007 event, and from three GNSS stations (BYRL, CRIM, UWEV) for the March 2011 event. Step functions were fitted to GNSS time series and used to determine the mean change in east, north and vertical displacements for both events and their associated standard deviations (Fig. S7). Displacement data recorded during the event (a 48-h period centred on the maximum change of displacement) were excluded from statistical analyses. We incorporate effects of GNSS measurement uncertainty by taking a Gaussian sample ($n = 100$, values in Table S8) for each displacement component, at each station. Mogi and McTigue models assume radial homogeneity, so all GNSS-derived east and north displacements were rotated into horizontal-radial components, using the location of the Halema'uma'u Reservoir inferred by Anderson et al. (2015). These results are displayed in Fig. S8.

The summit deformation during these intrusive events is attributed to a decrease in source overpressure. This change in source overpressure was calculated from radial tilt measurements at tiltmeter UWE at Kīlauea's summit. Tilt data were solely used for this purpose; only GNSS data were considered within deformation analyses. The change in tilt for each event was defined as the difference in radial tilt at UWE across the same 'before' and 'after' time periods used within GNSS data analyses. Table S6 contains these data. Prior to 2018, surface deformation at Kīlauea's summit correlated linearly with the level of the lava lake, which had a direct connection to the Halema'uma'u magma reservoir (Patrick et al., 2015). Consequently radial tilt measured at Kīlauea's summit could be used to directly estimate magma reservoir pressure. For a magma density of 1750 kg.m^{-3}, a change of 1μRad in radial tilt at UWE corresponds with an overpressure change of 0.086 MPa (Patrick et al., 2015). Using this methodology, the overpressure changes associated with the events in June 2007 and March 2011 were $\Delta P = -3.73$ and -3.55 MPa respectively.

As before, we use a simple elastic, homogeneous domain with a flat free surface. Model parameters are defined in Table 3. The high temperature of the Halema'uma'u Reservoir will cause surrounding rocks to have temperatures above the brittle-ductile transition, and consequently have a viscoelastic component to their behaviour. However, over the short time periods we investigate, the elastic component of the material's response will dominate (e.g. Head et al., 2019), such that the assumption of elasticity is an appropriate simplification. Heterogeneities, including faults, fractures and layering affect deformation

Table 3
Model parameters for two intrusion events at Kīlauea.

	Symbol	Definition	Units	Value(s)
Domain parameters	G	Shear modulus	GPa	4.0
	ν	Poisson's ratio	–	0.25
Source parameters	ΔP	Overpressure	MPa	−3.73, −3.55
	a	Radius	km	0.40 − 1.10
	d	Depth	km	1.00 − 3.00

The domain is homogeneous, elastic and has a flat free surface and sources are spherical. Source overpressures are inferred from tilt measurements; −3.73 and − 3.55 MPa are overpressures for events in June 2007 and March 2011 respectively. 50 equally-spaced values of source radius and depth are tested.

(e.g. Manconi et al., 2007), and consequently the inferred deformation source parameters (e.g. Segall, 2019). However, accurately constraining small-scale heterogeneities, such as those which could be incorporated within our local-scale models, would require geophysical survey data to be collected at unfeasibly high-resolution. Consequently, the assumption of homogeneity is appropriate. Topography has a smaller effect on the deformation field than other Mogi assumptions, including homogeneity (Masterlark, 2007), although variation in elevation height (and thus source-surface separation) and the presence of steep slopes affect the displacement field (Cayol and Cornet, 1998; Williams and Wadge, 1998). Our models are concerned with only the summit of Kīlauea; GNSS stations are separated by less than 4 km and are located on ground at similar elevation, and with similar slope steepness. Thus, assuming a flat free surface is appropriate.

A grid search is used within Mogi, McTigue and FE models to define the best-fitting combination of source radius and depth for each event. Source radius is varied between 0.40 and 1.10 km (95% confidence interval of Anderson et al., 2015), and source depth, which is relatively poorly constrained (e.g. Anderson et al., 2015), is varied between 1.0 and 3.0 km, a probable depth range for the Halema'uma'u Reservoir (e.g. Lundgren et al., 2013; Poland et al., 2014; Anderson et al., 2015; Neal et al., 2019). This gives tested radius-depth ratios upwards of 0.13. 50 equally-spaced values of source radius and depth are evaluated (2500 combinations in total, Table 3 for model parameters). Results are ignored where values of source radius and depth are incompatible.

4.6. Kīlauea modelling: results

Using synthetic data, we found correspondence between analytical and numerical models differed with the displacement component (*Ur* or *Uz*) that was analysed. To consider the validity of this conclusion when using observational data, we continue evaluating results inferred using radial and vertical displacement components independently and simultaneously. Thus, for each model (Mogi, McTigue and FE), the misfit between modelled and observed radial and vertical displacement components was computed at each GNSS station, for each radius-depth combination within the Gaussian sample. These results were summed, giving radial, M_r, vertical, M_z, and radial and vertical, M_{rz} misfits. For example, given radius-depth combination r_1, d_1:

$$M_r(r_1,d_1)=\sum_i\left[\frac{(Ur_i(r_1,d_1)-Dr_i)}{\sigma r_i}\right]^2 \tag{14}$$

$$M_z(r_1,d_1)=\sum_i\left[\frac{(Uz_i(r_1,d_1)-Dz_i)}{\sigma z_i}\right]^2 \tag{15}$$

$$M_{rz}(r_1,d_1)=M_r(r_1,d_1)+M_z(r_1,d_1) \tag{16}$$

where Ur_i and Uz_i are the modelled horizontal-radial and vertical displacement components, Dr_i and Dz_i are the GNSS observations and σr_i and σz_i are the associated uncertainties. i indicates the GNSS stations being considered. Misfits were computed for both June 2007 (i denoting results from stations BYRL and UWEV) and March 2011 events (i denoting results from stations BYRL, CRIM and UWEV). Misfits from the two events were also summed for combined M_r, M_z, and M_{rz}.

For each observed displacement (within the Gaussian sample), we computed the best-fitting source radius and depth combination, for Mogi, McTigue and FE models (Fig. 8). There are clear differences in the values and range of best-fitting radius-depth combinations depending on whether *Ur* and *Uz* are evaluated independently or simultaneously, but little difference between results obtained using Mogi, McTigue and FE models.

To compare the optimum source radii and depths for each model, we conducted statistical analyses on the best-fitting 5% of radius-depth combinations inferred using Mogi, McTigue and FE models (Table S4). Using Kruskal-Wallis and post-hoc Dunn's tests, we tested for differences between the best-fitting Mogi, McTigue and FE source radii and depths. A Bonferroni correction was applied to p-values to account for multiple comparisons, and a significance level of 0.05 was used (all statistical results in Table S5).

We found no difference between the best-fitting source radii or depths inferred using FE and McTigue models, regardless of which displacement component (*Ur* or *Uz* or *Ur* and *Uz*) or which event (June 2007, March 2011 or combined) were tested (Fig. 9). Comparing FE and Mogi models, we found significant differences in the inferred source radii, but fewer differences in the best-fitting source depths. For the June 2007 event, source radii inferred using the Mogi model were significantly greater than radii inferred using FE or McTigue models ($p < 0.002$); the Mogi model underestimates surface deformations produced by deformation sources with larger radii. Correspondence between Mogi and FE models also depended on the direction of displacement data that were evaluated. Differences between inferred source depth only differed between these two models when horizontal-radial displacement components (*Ur*) were considered; there were no differences when source depths were inferred using only the vertical (*Uz*), or the combined (*Ur* and *Uz*) displacement components.

The final stage of our analyses is a comparison of the modelled and observed surface displacement vectors. We select the 124 (5%) of radius-depth combinations with the smallest $\overline{M}_{rz}$ for FE models. The horizontal-radial and vertical displacement components produced by these sources within Mogi, McTigue and FE models were compared to the Gaussian sample of GNSS observations (Fig. 10, Figs. S8 and S9 display results for each model separately). There are good correspondences between all models, but for some stations there are relatively poor correspondences between model- and GNSS-derived displacements. In June 2007, both *Ur* and *Uz* at station UWEV correspond with GNSS observations. However, at station BYRL *Uz* are underestimated, and there is discrepancy between the direction of the displacement vector; GNSS observations are not oriented radially to the Halema'uma'u Reservoir, whereas the three models simulate only radial displacements. This is a limitation of applying simple analytical models to complex volcanic systems. In March 2011, there is good correspondence between *Ur* at BYRL and CRIM, but *Ur* are underestimated by all three models at UWEV. Conversely, the modelled and observed *Uz* at station UWEV correspond, but at CRIM and UWEV the modelled *Uz* are over- and underestimated respectively.

4.7. Kīlauea modelling: conclusions

GNSS-derived surface displacement data from two intrusive events at Kīlauea Volcano were interpreted using Mogi, McTigue and FE models to quantify how inferences made using these three models differ. This procedure yields similar results as for synthetic data. Firstly, there is good correspondence between Mogi and FE models, even when $\varepsilon \not\ll 1$

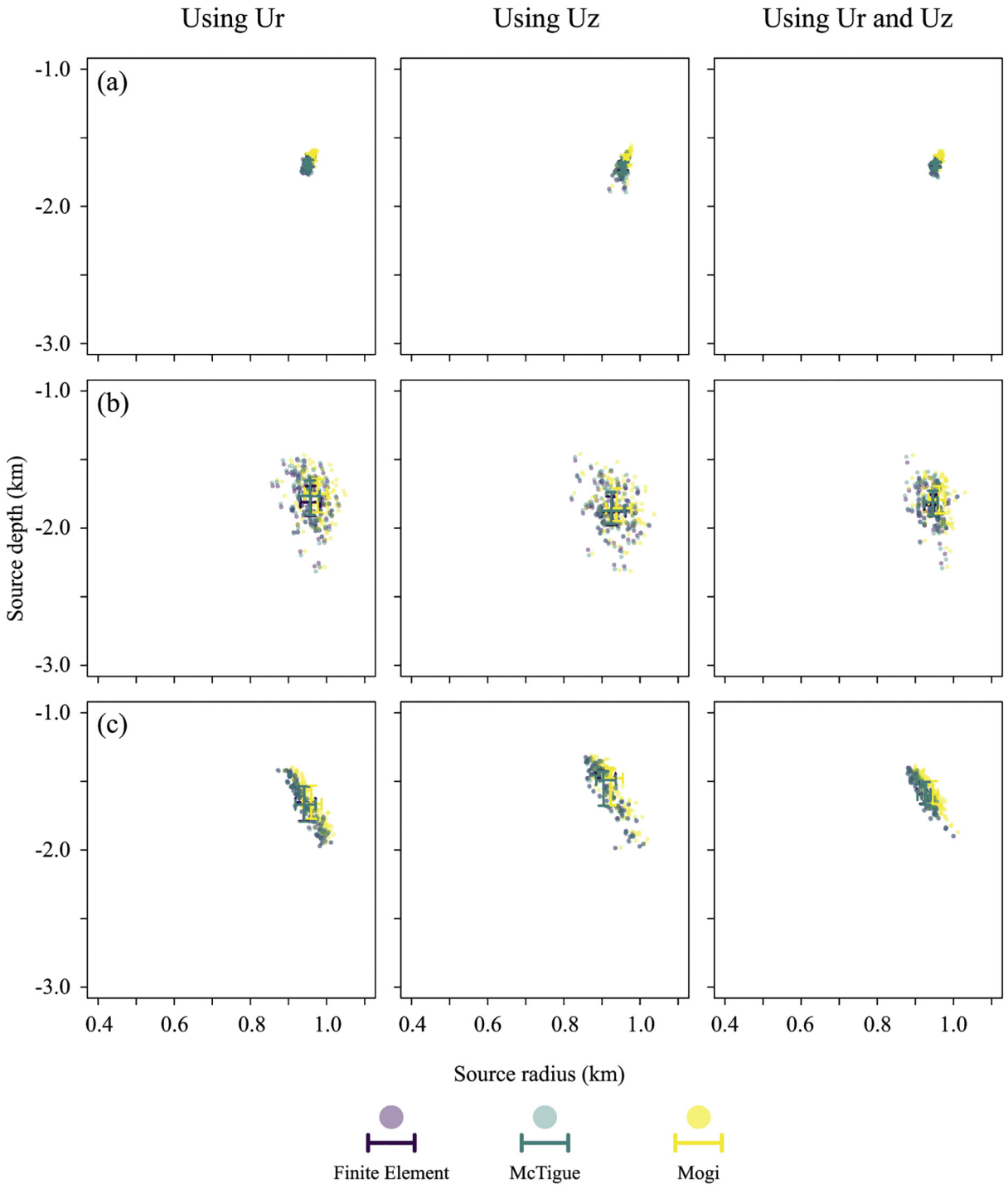

Fig. 8. Best-fitting radius-depth combinations for three models using horizontal-radial (*Ur*), vertical (*Uz*) and combined (*Ur* and *Uz*) displacements. (a) June 2007 event, (b) March 2011 event and (c) June 2007 and March 2011 events combined. Each point represents the mean of the best-fitting 5% of radius-depth combinations ($n = 124$); one point for each of the GNSS observations within the Gaussian sample ($n = 100$). Error bars indicate the mean and standard deviation of all sampled GNSS observations.

(best-fitting radius-depth combinations had $\varepsilon < 0.73$), but the correspondence is better between McTigue and FE models. Second, where Mogi and FE models differed, the Mogi models overestimated source radius - the Mogi model underestimates the magnitude of the displacement field. Third, there is better agreement between Mogi and FE models when the horizontal-radial component of displacement data are evaluated, compared to when either vertical data, or combined horizontal-radial and vertical components are evaluated. These results also demonstrate the limitations of Mogi and McTigue models. There was a lack of correspondence between GNSS observations and model results at some stations, which is attributed to the assumptions of homogeneity, flat topography and elasticity made within these simple models. For our simulations, the presence of steep cliffs around Kīlauea's summit caldera is likely to have a particularly significant effect on the displacement field (Johnson et al., 2019), but when Mogi and McTigue models are applied elsewhere, particularly for assessing surface displacements over larger areas and over greater time periods, the neglection of heterogeneity and

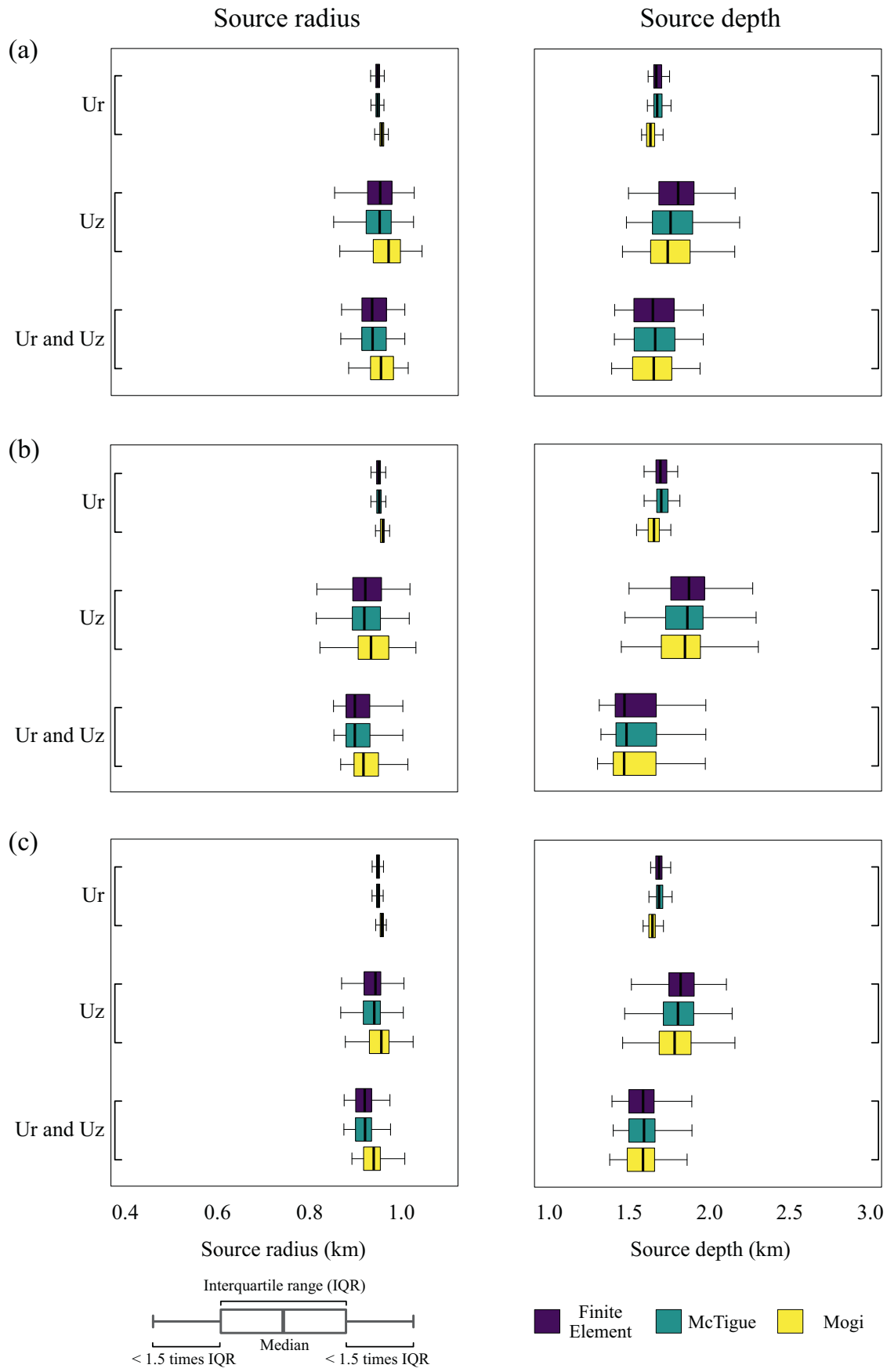

Fig. 9. Best-fitting source radius and depth combinations for Mogi, McTigue and FE models. (a) June 2007 event, (b) March 2011 event and (c) June 2007 and March 2011 events combined. Results are for the radius-depth combinations within the smallest 5% of misfits averaged across all of the sampled GNSS observations.

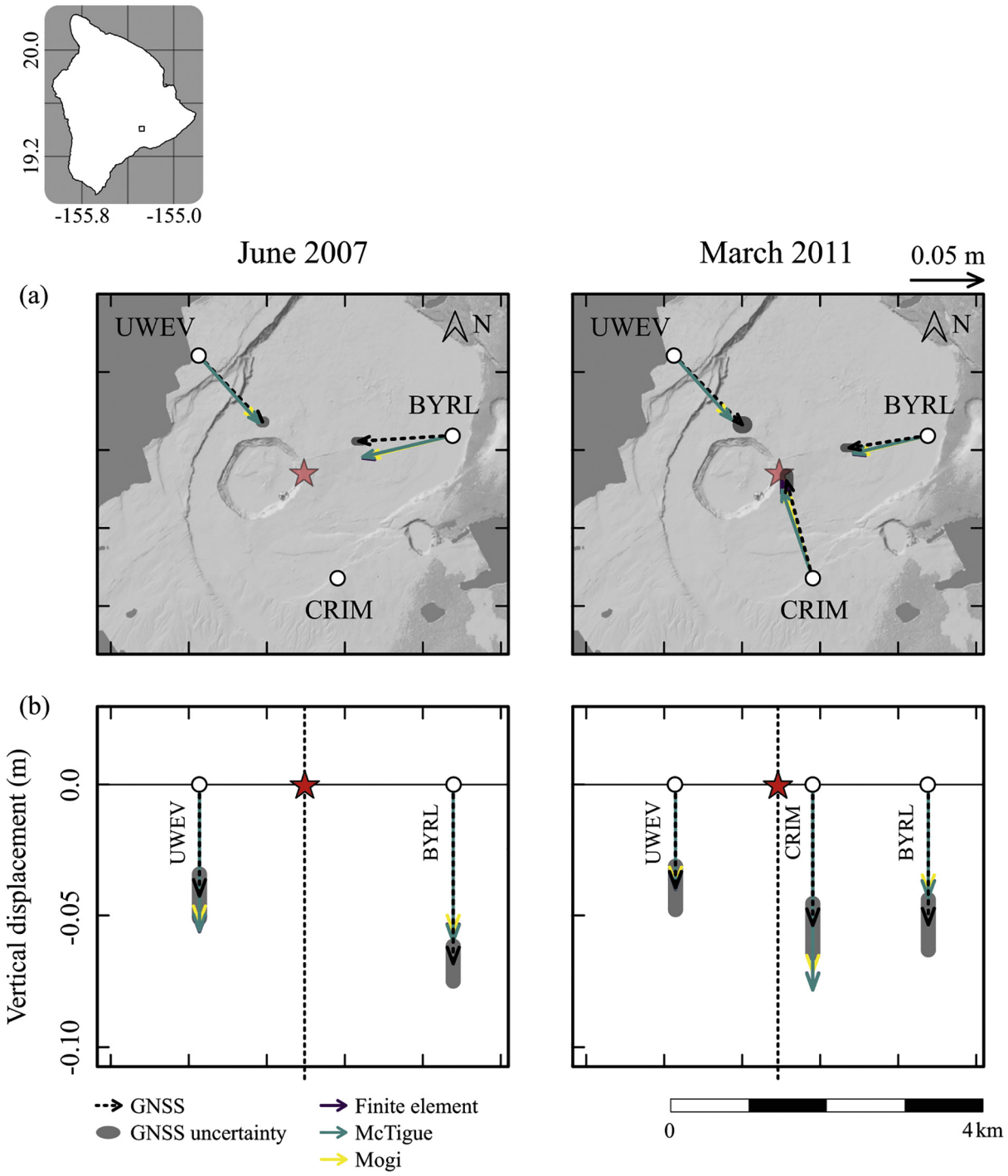

Fig. 10. Displacement vectors (horizontal-radial (a) and vertical (b)) produced within Mogi, McTigue and FE models for the 5% of radius-depth combinations that, for FE models, had the smallest misfit to observations. Study area indicated on inset. Shaded ellipses show the GNSS-derived displacements, ranges are the mean value ± one standard deviation. Model results (coloured arrows) are the average of the best-fitting 5% of radius-depth combinations, averaged across all sampled GNSS observations. The red star is the surface location of the Halema'uma'u reservoir. Figs. S8 and S9 display all displacement vectors for all best-fitting radius-depth combinations. (For interpretation of the references to colour in this figure legend, the reader is referred to the web version of this article.)

viscoelasticity may also be significant (e.g. Masterlark, 2007; Del Negro et al., 2009).

5. Conclusions

In this study we tested the correspondence between two simple analytical models - Mogi and McTigue - and FE models for deformation sources with a range of radius to depth ratios. We quantified the limits of applicability of these simple yet widely-used analytical models, and provide guidance for their application when interpreting deformation data and benchmarking more complex models. This correspondence was tested for forward and inverse analyses of synthetic displacement data, and for estimating source parameters during GNSS-observed unrest episodes at Kīlauea Volcano.

The Mogi model simplifies deformation sources to small sphere anomalies, necessitating $\varepsilon \ll 1$. The McTigue model extends the Mogi

model, providing a higher-order correction to account for the effects of a spherical deformation source with finite dimensions. We found that the Mogi model performed better than expected for $\varepsilon \not\ll 1$. The misfit between Mogi and FE models was less than 5% for $\varepsilon < 0.37$, but when we modelled events at Kīlauea we found correspondence between source properties estimated using Mogi and FE models even when $\varepsilon \approx 0.7$. For relatively minor additional computational cost, the McTigue model provides improved correspondence with FE models for large ε. The misfit between McTigue and FE models was less than 5% for $\varepsilon < 0.59$, and there was no difference between source parameters inferred at Kīlauea using McTigue and FE models.

Using only ε to determine the limit of applicability of analytical models may be an oversimplification. Mogi and McTigue models are better at predicting displacement components from, and inferring source properties of, deformation sources at shallow depths than those with large radii. The correspondence between analytical and FE models also depends on the displacement component being evaluated. There is better agreement between source parameters inferred using Mogi and FE models, and McTigue and FE models, when only the radial component of the displacement field is evaluated.

Application of simple analytical models to deformation observations will always be limited by the model's assumptions, particularly of elasticity, homogeneity and flat topography, and for our Kīlauea models, these simplifications restricted the correspondence between GNSS observations and model results. However, some of these complexities can be accounted for with relative ease within Mogi and McTigue models, such that, for many situations, these simple analytical models remain appropriate. Consequently, with the validation for the use of Mogi and McTigue models presented here, these simple models can provide a good solution for geodetic problems.

Declaration of Competing Interest

The authors declare that they have no known competing financial interests or personal relationships that could have appeared to influence the work reported in this paper.

Acknowledgments

COMSOL models are available in the supporting information. We thank editor D. Roman and three anonymous reviewers for their comments that have improved this manuscript. We thank Michael Poland for his helpful and insightful discussions, and Jade Eyles and Bridie Davies for support throughout the project. We thank the staff of the USGS Hawaiian Volcano Observatory for provision of GNSS time series. GNSS data are available from unavco.org (Miklius, 2018a, 2018b; Segall and Miklius, 2018) from continuously operating GNSS stations operated by the USGS Hawaiian Volcano Observatory. N.T. is supported by the Natural Environment Research Council through the EnvEast Doctoral Training Partnership (NE/L002582/1).

Appendix A. Supplementary data

Supplementary data to this article can be found online at https://doi.org/10.1016/j.jvolgeores.2021.107380.

References

Amelung, F., Jonsson, S., Zebker, H., Segall, P., Oct. 2000. Widespread uplift and 'trapdoor' faulting on Galapagos volcanoes observed with radar interferometry. Nature 407, 4.

Anderson, K., Segall, P., Jul. 2011. Physics-based models of ground deformation and extrusion rate at effusively erupting volcanoes. J. Geophys. Res. 116 (B7), B07204 URL. http://doi.wiley.com/10.1029/2010JB007939.

Anderson, K.R., Poland, M.P., Johnson, J.H., Miklius, A., Feb. 2015. Episodic deflation-inflation events at Kīlauea Volcano and implications for the shallow magma system. In: Carey, R., Cayol, V., Poland, M., Weis, D. (Eds.), Geophysical Monograph Series. John Wiley & Sons, Inc, Hoboken, NJ , pp. 229–250 URL. http://doi.wiley.com/10.1002/9781118872079.ch11.

Baker, S., Amelung, F., Dec. 2012. Top-down inflation and deflation at the summit of Kīlauea Volcano, Hawai'i observed with InSAR. J. Geophys. Res. Solid Earth 117 (B12), B12406 URL. http://doi.wiley.com/10.1029/2011JB009123.

Becerril, L., Galindo, I., Gudmundsson, A., Morales, J.M., Dec. 2013. Depth of origin of magma in eruptions. Sci. Rep. 3 (1), 2762 URL. http://www.nature.com/articles/srep02762.

Biggs, J., Ebmeier, S.K., Aspinall, W.P., Lu, Z., Pritchard, M.E., Sparks, R.S.J., Mather, T.A., May 2014. Global link between deformation and volcanic eruption quantified by satellite imagery. Nat. Commun. 5 (1), 3471 URL. http://www.nature.com/articles/ncomms4471.

Bonaccorso, A., Mar. 1996. Dynamic inversion of ground deformation data for modelling volcanic sources (Etna 1991-93). Geophys. Res. Lett. 23 (5), 451–454 URL. http://doi.wiley.com/10.1029/96GL00418.

Bonaccorso, A., Cianetti, S., Giunchi, C., Trasatti, E., Bonafede, M., Boschi, E., Nov. 2005. Analytical and 3-D numerical modelling of Mt. Etna (Italy) volcano inflation. Geophys. J. Int. 163 (2), 852–862 URL. https://academic.oup.com/gji/article-lookup/doi/10.1111/j.1365-246X.2005.02777.x.

Carnec, C., Fabriol, H., May 1999. Monitoring and modeling land subsidence at the Cerro Prieto Geothermal Field, Baja California, Mexico, using SAR interferometry. Geophys. Res. Lett. 26 (9), 1211–1214 URL. http://doi.wiley.com/10.1029/1999GL900062.

Castaldo, R., Gola, G., Santilano, A., De Novellis, V., Pepe, S., Manzo, M., Manzella, A., Tizzani, P., Sep. 2017. The role of thermo-rheological properties of the crust beneath Ischia Island (Southern Italy) in the modulation of the ground deformation pattern. J. Volcanol. Geotherm. Res. 344, 154–173 URL. https://linkinghub.elsevier.com/retrieve/pii/S0377027317301397.

Cayol, V., Cornet, F.H., Jun. 1998. Effects of topography on the interpretation of the deformation field of prominent volcanoes-Application to Etna. Geophys. Res. Lett. 25 (11), 1979–1982 URL. http://doi.wiley.com/10.1029/98GL51512.

Chouet, B.A., Matoza, R.S., Feb. 2013. A multi-decadal view of seismic methods for detecting precursors of magma movement and eruption. J. Volcanol. Geotherm. Res. 252, 108–175 URL. https://linkinghub.elsevier.com/retrieve/pii/S0377027312003435.

Coco, A., Gottsmann, J., Whitaker, F., Rust, A., Currenti, G., Jasim, A., Bunney, S., Apr. 2016. Numerical models for ground deformation and gravity changes during volcanic unrest: simulating the hydrothermal system dynamics of a restless caldera. Solid Earth 7 (2), 557–577 URL. https://www.solid-earth.net/7/557/2016/.

Currenti, G., May 2018. Viscoelastic modeling of deformation and gravity changes induced by pressurized magmatic sources. J. Volcanol. Geotherm. Res. 356, 264–277 URL. https://linkinghub.elsevier.com/retrieve/pii/S0377027317304456.

Currenti, G., Bonaccorso, A., Del Negro, C., Scandura, D., Boschi, E., Aug. 2010. Elasto-plastic modeling of volcano ground deformation. Earth Planet. Sci. Lett. 296 (3-4), 311–318 URL. https://linkinghub.elsevier.com/retrieve/pii/S0012821X10003316.

Del Negro, C., Currenti, G., Scandura, D., Feb. 2009. Temperature-dependent viscoelastic modeling of ground deformation: application to Etna volcano during the 1993–1997 inflation period. Phys. Earth Planet. Inter. 172 (3-4), 299–309 URL. https://linkinghub.elsevier.com/retrieve/pii/S0031920108003087.

Delaney, P.T., McTigue, D.F., 1994. Volume of magma accumulation or withdrawal estimated from surface uplift or subsidence, with application to the 1960 collapse of Kīlauea Volcano. Bull. Volcanol. 56, 417–424.

Dieterich, J.H., Decker, R.W., Oct. 1975. Finite element modeling of surface deformation associated with volcanism. J. Geophys. Res. 80 (29), 4094–4102 URL. http://doi.wiley.com/10.1029/JB080i029p04094.

Eckl, M.C., Snay, R.A., Soler, T., Cline, M.W., Mader, G.L., Dec. 2001. Accuracy of GPS-derived relative positions as a function of interstation distance and observing-session duration. J. Geod. 75 (12), 633–640 URL. http://link.springer.com/10.1007/s001900100204.

Edmonds, M., Sides, I., Swanson, D., Werner, C., Martin, R., Mather, T., Herd, R., Jones, R., Mead, M., Sawyer, G., Roberts, T., Sutton, A., Elias, T., Dec. 2013. Magma storage, transport and degassing during the 2008–10 summit eruption at Kīlauea Volcano, Hawai'i. Geochim. Cosmochim. Acta 123, 284–301 URL. https://linkinghub.elsevier.com/retrieve/pii/S0016703713003256.

Edmonds, M., Cashman, K.V., Holness, M., Jackson, M., Feb. 2019. Architecture and dynamics of magma reservoirs. Philos. Trans. R. Soc. A Math. Phys. Eng. Sci. 377 (2139), 20180298 URL. http://www.royalsocietypublishing.org/doi/10.1098/rsta.2018.0298.

Garcia, M.O., Feb. 2015. How and why Hawaiian volcanism has become pivotal to our understanding of volcanoes from their source to the surface. In: Carey, R., Cayol, V., Poland, M., Weis, D. (Eds.), Geophysical Monograph Series. John Wiley & Sons, Inc, Hoboken, NJ , pp. 1–18 URL. http://doi.wiley.com/10.1002/9781118872079.ch1.

Geyer, A., Gottsmann, J., Mar. 2010. The influence of mechanical stiffness on caldera deformation and implications for the 1971–1984 Rabaul uplift (Papua New Guinea). Tectonophysics 483 (3-4), 399–412 URL. https://linkinghub.elsevier.com/retrieve/pii/S004019510900626X.

Grosfils, E.B., Oct. 2007. Magma reservoir failure on the terrestrial planets: assessing the importance of gravitational loading in simple elastic models. J. Volcanol. Geotherm. Res. 166 (2), 47–75 URL. https://linkinghub.elsevier.com/retrieve/pii/S0377027307001941.

Gubbins, D., 2004. Time Series Analysis and Inverse Theory for Geophysicists. Cambridge University Press, Cambridge, UK.

Hautmann, S., Gottsmann, J., Sparks, R.S.J., Mattioli, G.S., Sacks, I.S., Strutt, M.H., Sep. 2010. Effect of mechanical heterogeneity in arc crust on volcano deformation with application to Soufrière Hills Volcano, Montserrat, West Indies. J. Geophys. Res. 115 (B9), B09203 URL. http://doi.wiley.com/10.1029/2009JB006909.

Head, M., Hickey, J., Gottsmann, J., Fournier, N., Aug. 2019. The influence of viscoelastic crustal rheologies on volcanic ground deformation: insights from models of pressure and volume change. J. Geophys. Res. Solid Earth 124 (8), 8127–8146 2019JB017832. URL. https://onlinelibrary.wiley.com/doi/abs/10.1029/2019JB017832.

Henderson, S.T., Pritchard, M.E., Dec. 2017. Time-dependent deformation of Uturuncu volcano, Bolivia, constrained by GPS and InSAR measurements and implications for source models. Geosphere 13 (6), 1834–1854 URL. https://pubs.geoscienceworld.org/geosphere/article-lookup?doi=10.1130/GES01203.1.

Hickey, J., Gottsmann, J., Jun. 2014. Benchmarking and developing numerical Finite Element models of volcanic deformation. J. Volcanol. Geotherm. Res. 280, 126–130 URL. https://linkinghub.elsevier.com/retrieve/pii/S037702731400153X.

Hickey, J., Gottsmann, J., del Potro, R., Mar. 2013. The large-scale surface uplift in the Altiplano-Puna region of Bolivia: a parametric study of source characteristics and crustal rheology using finite element analysis. Geochem. Geophys. Geosyst. 14 (3), 540–555 URL. http://doi.wiley.com/10.1002/ggge.20057.

Hickey, J., Gottsmann, J., Nakamichi, H., Iguchi, M., Dec. 2016. Thermomechanical controls on magma supply and volcanic deformation: application to Aira caldera, Japan. Sci. Rep. 6 (1), 32691 URL. http://www.nature.com/articles/srep32691.

Hickey, J., Gottsmann, J., Mothes, P., Odbert, H., Prutkin, I., Vajda, P., 2017. The ups and downs of volcanic unrest: insights from integrated geodesy and numerical modelling. In: Gottsmann, J., Neuberg, J., Scheu, B. (Eds.), Volcanic Unrest. Springer International Publishing, Cham , pp. 203–219 URL. http://link.springer.com/10.1007/11157_2017_13.

Johnson, D.J., Sigmundsson, F., Delaney, P.T., 2000. Comment on "Volume of magma accumulation or withdrawal estimated from surface uplift or subsidence, with application to the 1960 collapse of Kīlauea Volcano" by P. T. Delaney and D. F. McTigue. Bull. Volcanol. 61, 491–493.

Johnson, D.J., Eggers, A.A., Bagnardi, M., Battaglia, M., Poland, M.P., Miklius, A., Jul. 2010. Shallow magma accumulation at Kīlauea Volcano, Hawai'i, revealed by microgravity surveys. Geology 38 (12), 1139–1142.

Johnson, J.H., Poland, M.P., Anderson, K.R., Biggs, J., Apr. 2019. A cautionary tale of topography and tilt from Kīlauea Caldera. Geophys. Res. Lett. 46 (8), 4221–4229 URL. https://onlinelibrary.wiley.com/doi/abs/10.1029/2018GL081757.

Liang, C., Dunham, E.M., Apr. 2020. Lava lake sloshing modes during the 2018 Kīlauea Volcano eruption probe magma reservoir storativity. Earth Planet. Sci. Lett. 535, 116110 URL. https://linkinghub.elsevier.com/retrieve/pii/S0012821X20300534.

Lin, G., Shearer, P.M., Matoza, R.S., Okubo, P.G., Amelung, F., May 2014. Three-dimensional seismic velocity structure of Mauna Loa and Kilauea volcanoes in Hawaii from local seismic tomography. J. Geophys. Res. Solid Earth 119 (5), 4377–4392 URL. http://doi.wiley.com/10.1002/2013JB010820.

Lisowski, M., 2007. Analytical volcano deformation source models. Volcano Deformation. Springer Berlin Heidelberg, Berlin, Heidelberg , pp. 279–304 URL. http://link.springer.com/10.1007/978-3-540-49302-0_8.

Liu, P., Li, Q., Li, Z., Hoey, T., Liu, G., Wang, C., Hu, Z., Zhou, Z., Singleton, A., Mar. 2016. Anatomy of subsidence in Tianjin from time series InSAR. Remote Sens. 8 (3), 266 URL. http://www.mdpi.com/2072-4292/8/3/266.

Lundgren, P., Poland, M., Miklius, A., Orr, T., Yun, S.-H., Fielding, E., Liu, Z., Tanaka, A., Szeliga, W., Hensley, S., Owen, S., Mar. 2013. Evolution of dike opening during the March 2011 Kamoamoa fissure eruption, Kīlauea Volcano, Hawai'i. J. Geophys. Res. Solid Earth 118 (3), 897–914 URL. http://doi.wiley.com/10.1002/jgrb.50108.

Manconi, A., Walter, T.R., Amelung, F., Aug. 2007. Effects of mechanical layering on volcano deformation. Geophys. J. Int. 170 (2), 952–958 URL. https://academic.oup.com/gji/article-lookup/doi/10.1111/j.1365-246X.2007.03449.x.

Masterlark, T., Jun. 2007. Magma intrusion and deformation predictions: sensitivities to the Mogi assumptions. J. Geophys. Res. 112 (B6), B06419 URL. http://doi.wiley.com/10.1029/2006JB004860.

Masterlark, T., Tung, S., Jul. 2018. Finite element models of elastic volcano deformation. In: Aiello, G. (Ed.), Volcanoes – Geological and Geophysical Setting, Theoretical Aspects and Numerical Modeling, Applications to Industry and their Impact on the Human Health. InTech URL. http://www.intechopen.com/books/volcanoes-geological-and-geophysical-setting-theoretical-aspects-and-numerical-modeling-applications-to-industry-and-their-impact-on-the-human-health/finite-element-models-of-elastic-volcano-deformation.

Masterlark, T., Feigl, K.L., Haney, M., Stone, J., Thurber, C., Ronchin, E., Feb. 2012. Nonlinear estimation of geometric parameters in FEMs of volcano deformation: Integrating tomography models and geodetic data for Okmok volcano, Alaska. J. Geophys. Res. Solid Earth 117 (B2), B02047 URL. http://doi.wiley.com/10.1029/2011JB008811.

McTigue, D.F., 1987. Elastic stress and deformation near a finite spherical magma body: resolution of the point source paradox. J. Geophys. Res. 92 (B12), 12931 URL. http://doi.wiley.com/10.1029/JB092iB12p12931.

Miklius, A., 2018a. Hawaii GPS Network - BYRL-Byrons Ledge P.S. Type: Dataset. Aug. 2018. URL. https://www.unavco.org/data/doi/10.7283/T5NZ85W4.

Miklius, A., 2018b. Hawaii GPS Network - CRIM-Crater Rim P.S. Type: Dataset. Aug. 2018. URL. https://www.unavco.org/data/doi/10.7283/T5RR1WGN.

Mogi, K., 1958. Relations between the eruptions of various volcanoes and the deformations of the ground surfaces around them. Bull. Earthq. Res. Inst. 36, 99–134.

Neal, C.A., Brantley, S.R., Antolik, L., Babb, J.L., Burgess, M., Calles, K., Cappos, M., Chang, J.C., Conway, S., Desmither, L., Dotray, P., Elias, T., Fukunaga, P., Fuke, S., Johanson, I.A., Kamibayashi, K., Kauahikaua, J., Lee, R.L., Pekalib, S., Miklius, A., Million, W., Moniz, C.J., Nadeau, P.A., Okubo, P., Parcheta, C., Patrick, M.R., Shiro, B., Swanson, D.A., Tollett, W., Trusdell, F., Younger, E.F., Zoeller, M.H., Montgomery-Brown, E.K., Anderson, K.R., Poland, M.P., Ball, J.L., Bard, J., Coombs, M., Dietterich, H.R., Kern, C., Thelen, W.A., Cervelli, P.F., Orr, T., Houghton, B.F., Gansecki, C., Hazlett, R., Lundgren, P., Diefenbach, A.K., Lerner, A.H., Waite, G., Kelly, P., Clor, L., Werner, C., Mulliken, K., Fisher, G., Damby, D., Jan. 2019. The 2018 rift eruption and summit collapse of Kīlauea Volcano. Science 363 (6425), 367–374 URL. http://www.sciencemag.org/lookup/doi/10.1126/science.aav7046.

Neuberg, J.W., Collinson, A.S., Mothes, P.A.C., Ruiz, M., Aguaiza, S., Jan. 2018. Understanding cyclic seismicity and ground deformation patterns at volcanoes: intriguing lessons from Tungurahua volcano, Ecuador. Earth Planet. Sci. Lett. 482, 193–200 URL. https://linkinghub.elsevier.com/retrieve/pii/S0012821X17306180.

Newman, A.V., Dixon, T.H., Gourmelen, N., Feb. 2006. A four-dimensional viscoelastic deformation model for Long Valley Caldera, California, between 1995 and 2000. J. Volcanol. Geotherm. Res. 150 (1–3), 244–269 URL. https://linkinghub.elsevier.com/retrieve/pii/S0377027305002647.

Orr, T.R., Poland, M.P., Patrick, M.R., Thelen, W.A., Sutton, A.J., Elias, T., Thornber, C.R., Parcheta, C., Wooten, K.M., Feb. 2015. Kīlauea's 5-9 March 2011 Kamoamoa Fissure Eruption and its relation to 30+ years of activity from Pu'u 'Ō 'ō. In: Carey, R., Cayol, V., Poland, M., Weis, D. (Eds.), Geophysical Monograph Series. John Wiley & Sons, Inc, Hoboken, NJ, pp. 393–420 URL. http://doi.wiley.com/10.1002/9781118872079.ch18.

Pascal, K., Neuberg, J., Rivalta, E., Jan. 2014. On precisely modelling surface deformation due to interacting magma chambers and dykes. Geophys. J. Int. 196 (1), 253–278 URL. https://academic.oup.com/gji/article/196/1/253/585883.

Patrick, M.R., Anderson, K.R., Poland, M.P., Orr, T.R., Swanson, D.A., Sep. 2015. Lava lake level as a gauge of magma reservoir pressure and eruptive hazard. Geology 43 (9), 831–834 URL. https://pubs.geoscienceworld.org/geology/article/43/9/831-834/131980.

Patrick, M., Orr, T., Swanson, D., Lev, E., Dec. 2016. Shallow and deep controls on lava lake surface motion at Kīlauea Volcano. J. Volcanol. Geotherm. Res. 328, 247–261 URL. https://linkinghub.elsevier.com/retrieve/pii/S0377027316304590.

Patrick, M., Swanson, D., Orr, T., Mar. 2019. A review of controls on lava lake level: insights from Halema'uma'u Crater, Kīlauea Volcano. Bull. Volcanol. 81 (3), 13 URL. http://link.springer.com/10.1007/s00445-019-1268-y.

Pinel, V., Poland, M., Hooper, A., Dec. 2014. Volcanology: lessons learned from Synthetic Aperture Radar imagery. J. Volcanol. Geotherm. Res. 289, 81–113 URL. https://linkinghub.elsevier.com/retrieve/pii/S0377027314003084.

Poland, M.P., Carbone, D., Jul. 2016. Insights into shallow magmatic processes at Kīlauea Volcano, Hawai'i, from a multiyear continuous gravity time series. J. Geophys. Res. Solid Earth 121 (7), 5477–5492 URL. http://doi.wiley.com/10.1002/2016JB013057.

Poland, M.P., Miklius, A., Montgomery-Brown, E.K., 2014. Magma supply, storage, and transport at shield-stage Hawaiian volcanoes. Characteristics of Hawaiian Volcanoes. U.S. Geological Survey Vol. 1801 of U.S. Geological Survey Professional paper. p. 429.

Pritchard, M.E., Biggs, J., Wauthier, C., Sansosti, E., Arnold, D.W.D., Delgado, F., Ebmeier, S.K., Henderson, S.T., Stephens, K., Cooper, C., Wnuk, K., Amelung, F., Aguilar, V., Mothes, P., Macedo, O., Lara, L.E., Poland, M.P., Zoffoli, S., Dec. 2018. Towards coordinated regional multi-satellite InSAR volcano observations: results from the Latin America pilot project. J. Appl. Volcanol. 7 (1), 5 URL. https://appliedvolc.biomedcentral.com/articles/10.1186/s13617-018-0074-0.

Puglisi, G., Bonforte, A., Nov. 2004. Dynamics of Mount Etna Volcano inferred from static and kinematic GPS measurement. J. Geophys. Res. Solid Earth 109 (B11) URL. http://doi.wiley.com/10.1029/2003JB002878.

Rapp, B.E., 2017. Finite element method. Microfluidics: Modelling, Mechanics and Mathematics. Micro and Nano Technologies. Elsevier, Oxford, United Kingdom, pp. 655–678.

Segall, P., Feb. 2019. Magma chambers: what we can, and cannot, learn from volcano geodesy. Philos. Trans. R. Soc. A Math. Phys. Eng. Sci. 377 (2139), 20180158 URL. http://www.royalsocietypublishing.org/doi/10.1098/rsta.2018.0158.

Segall, P., Miklius, A., Aug. 2018. Hawaii GPS Network - UWEV-Uwekahuna Vault P.S. Type: Dataset. URL. https://www.unavco.org/data/doi/10.7283/T51C1TXB.

Sparks, R., May 2003. Forecasting volcanic eruptions. Earth Planet. Sci. Lett. 210 (1-2), 1–15 URL. https://linkinghub.elsevier.com/retrieve/pii/S0012821X03001249.

Tiampo, K.F., González, P.J., Samsonov, S., Fernández, J., Camacho, A., Sep. 2017. Principal component analysis of MSBAS DInSAR time series from Campi Flegrei, Italy. J. Volcanol. Geotherm. Res. 344, 139–153 URL. https://linkinghub.elsevier.com/retrieve/pii/S0377027317301439.

Trasatti, E., Giunchi, C., Agostinetti, N.P., Feb. 2008. Numerical inversion of deformation caused by pressure sources: application to Mount Etna (Italy). Geophys. J. Int. 172 (2), 873–884 URL. https://academic.oup.com/gji/article-lookup/doi/10.1111/j.1365-246X.2007.03677.x.

Widiwijayanti, C., 2005. Geodetic constraints on the shallow magma system at Soufrière Hills Volcano, Montserrat. Geophys. Res. Lett. 32 (11), L11309 URL. http://doi.wiley.com/10.1029/2005GL022846.

Williams, C.A., Wadge, G., May 1998. The effects of topography on magma chamber deformation models: Application to Mt. Etna and radar interferometry. Geophys. Res. Lett. 25 (10), 1549–1552 URL. http://doi.wiley.com/10.1029/98GL01136.

Zhan, Y., Gregg, P.M., Chaussard, E., Aoki, Y., Dec. 2017. Sequential assimilation of volcanic monitoring data to quantify eruption potential: application to Kerinci Volcano, Sumatra. Front. Earth Sci. 5, 108 URL. http://journal.frontiersin.org/article/10.3389/feart.2017.00108/full.